COMPARISON OF TURBULENCE MODEL AND WALL FUNCTION COUPLINGS FOR SIMULATING SCOUR

A THESIS SUBMITTED TO
THE GRADUATE SCHOOL OF NATURAL AND APPLIED SCIENCES
OF
MIDDLE EAST TECHNICAL UNIVERSITY

BY

BARIŞ UFUK ŞENTÜRK

IN PARTIAL FULFILLMENT OF THE REQUIREMENTS
FOR
THE DEGREE OF MASTER OF SCIENCE
IN
CIVIL ENGINEERING

JANUARY 2022

Approval of the thesis:

COMPARISON OF TURBULENCE MODEL AND WALL FUNCTION COUPLINGS FOR SIMULATING SCOUR

submitted by **BARIŞ UFUK ŞENTÜRK** in partial fulfillment of the requirements for the degree of **Master of Science** i**n Civil Engineering, Middle East Technical University** by,

Prof. Dr. Halil Kalıpçılar
Dean, Graduate School of **Natural and Applied Sciences** _____

Prof. Dr. Erdem Canbay
Head of the Department, **Civil Engineering** _____

Assist. Prof. Dr. Cüneyt Baykal
Supervisor, **Civil Engineering, METU** _____

Examining Committee Members:

Prof. Dr. Ahmet Cevdet Yalçıner
Civil Engineering, METU _____

Assist. Prof. Dr. Cüneyt Baykal
Civil Engineering, METU _____

Prof. Dr. İsmail Yücel
Civil Engineering, METU _____

Assist. Prof. Dr. Gülizar Özyurt Tarakcıoğlu
Civil Engineering, METU _____

Assoc. Prof. Dr. Bergüzar Öztunalı Özbahçeci
Civil Engineering, IZTECH _____

Date: 19.01.2022

I hereby declare that all information in this document has been obtained and presented in accordance with academic rules and ethical conduct. I also declare that, as required by these rules and conduct, I have fully cited and referenced all material and results that are not original to this work.

Name Last name : Barış Ufuk Şentürk

Signature :

ABSTRACT

COMPARISON OF TURBULENCE MODEL AND WALL FUNCTION COUPLINGS FOR SIMULATING SCOUR

Şentürk, Barış Ufuk
Master of Science, Civil Engineering
Supervisor: Assist. Prof. Dr. Cüneyt Baykal

January 2022, 92 pages

In this study, the scouring of bed material at the rear side of a rubble mound coastal revetment due to the overtopping of solitary-like waves is numerically studied using a coupled hydrodynamic and morphological computational fluid dynamics model. The major purpose of this thesis study is to investigate the performances of different turbulence model and wall function couplings on the hydrodynamic and morphological results. In the first part of this study, hydrodynamic simulations are performed, and the results are compared in terms of the free surface elevations, overtopping volumes, and jet thicknesses. It is concluded that the simulations that use laminar, k-ω, k-ω SST, and stabilized k-ω SST turbulence models show the best agreement with the experimental results. In contrast, the k-ε and standard k-ω simulations show the poor ones. Furthermore, it is observed that the use of different wall functions does not affect the hydrodynamic results significantly. In the second part of this study, morphological simulations are carried on, and the results are compared regarding the scour profiles, depths, lengths, and the distance of the deepest point to the crown wall. In conclusion, the k-ω turbulence model with Fuhrman et al. (2014) wall function simulation shows the best agreement with the

experimental result to capture the scour profile and depth. Furthermore, laminar, k-ω SST, stabilized k-ω SST, and k-ω with Fuhrman et al. (2014) wall function simulations match well with the experimental result regarding the scour length and the distance from the crown wall, while the other simulations do not show good agreements. It is also observed that suspended sediment transport is a significant contributor to the scour in the present study.

Keywords: Computational Fluid Dynamics, Porous Media Modeling, Turbulence Modeling, Wall Functions, Scour

ÖZ

TÜRBÜLANS MODELİ VE DUVAR FONKSİYONU EŞLEŞMELERİNİN OYULMA BENZETİMLERİ AÇISINDAN KIYASLANMASI

Şentürk, Barış Ufuk
Yüksek Lisans, İnşaat Mühendisliği
Tez Yöneticisi: Dr. Öğr. Üyesi Cüneyt Baykal

Ocak 2022, 92 sayfa

Bu çalışmada, soliter benzeri dalgaların aşmasından kaynaklanan taş dolgu kıyı tahkimat yapılarının arka tarafındaki dolgu malzemesinin oyulması, birleştirilmiş hidrodinamik ve morfolojik hesaplamalı akışkanlar dinamiği kodu kullanılarak sayısal olarak modellenmiştir. Bu çalışmanın esas amacı, farklı türbülans modeli ve duvar fonksiyonu eşleşmelerinin hidrodinamik ve morfolojik sonuçlara olan etkilerini araştırmaktır. Bu çalışmanın ilk bölümünde hidrodinamik benzetim çalışmaları yapılmış ve sonuçlar serbest su seviyesi, aşma miktarı ve aşan suyun jet kalınlığı açısından karşılaştırılmıştır. Sonuç olarak laminer, k-ω, k-ω SST ve stabilize k-ω SST türbülans modellerinin kulanıldığı benzetim çalışmaları, deney sonuçları ile uyumlu bulunmuştur. k-ε ve standart k-ω benzetimleri ise deney verileri ile zayıf düzeyde uyumlu bulunmuştur. Ayrıca, farklı duvar fonksiyonlarının kullanımının, hidrodinamik sonuçları etkilemediği gözlemlenmiştir. Bu çalışmanın ikinci bölümünde, morfolojik benzetim çalışmaları yapılmış ve sonuçlar oyulma profilleri, derinlikleri, uzunlukları ve en derin noktanın kronman duvarına olan uzaklığı açısından karşılaştırılmıştır. Sonuç olarak, k-ω türbülans modelini ve Fuhrman vd. (2014) tarafından sunulan duvar fonksiyonlarını kullanan benzetim çalışmasının deney verileri ile yüksek uyum sağladığı gözlemlenmiştir. Ayrıca,

laminer, k-ω SST, stabilize k-ω SST ve k-ω ile beraber kullanılan ve Fuhrman vd. (2014) tarafından sunulan duvar fonksiyonlu benzetim çalışmaları, oyulma uzunluğu ve kronman duvarına uzaklık açısından deney sonuçları ile uyumlu bulunurken diğer benzetim çalışmaları kötü sonuçlar göstermiştir. Ek olarak, bu çalışmada askıda kum taşınımının oyulmaya önemli bir etkisinin olduğu gözlemlenmiştir.

Anahtar Kelimeler: Hesaplamalı Akışkanlar Dinamiği, Gözenekli Ortam Akım Modellemesi, Türbülans Modellemesi, Duvar Fonksiyonları, Oyulma

To my family and my loved ones…

ACKNOWLEDGMENTS

I would like to express my sincere gratitude to my supervisor Assist. Prof. Dr. Cüneyt Baykal for his continuous support and suggestions. He always encouraged me and pushed me up during my thesis process. He always shared his knowledge with me and directed me to do my best. This thesis study might not be possible without his support.

I would like to express my sincere gratitude to Prof. Dr. Ayşen Ergin. It was a milestone for my career in this area to take a lecture from her at my undergraduate level. She always supported me to do my best with her smiling face. She instructed me on how to become a good academician as well as how to become a good person. It was an honor and luck to study with her.

I would like to express my sincere gratitude to Dr. Hasan Gökhan Güler. He always supported me in this study with his precious comments and answered my questions patiently. Besides my academic studies, he also helped me in my everyday life. I think I am fortunate to have a chance to work with him. Without his support, this study might not have been finished.

I want to express my special thanks to Prof. Dr. Ahmet Cevdet Yalçıner, Assist. Prof. Dr. Gülizar Özyurt Tarakcıoğlu and Dr. Işıkhan Güler. They always answered my questions and supported me to finish my study with their valuable comments. I am glad to become a member of this big family.

I would like to express my special thanks to Prof. Dr. Kağan Tuncay. His enthusiastic and competent attitude during the courses was very inspirational for me. The first lecture that I took was a milestone for my academic journey. With his inspiring comments, he always supported me. I appreciate his endless support.

I would like to express my special thanks to Assist. Prof. Dr. Bergüzar Öztunalı Özbahçeci. She accepted me as a student and directed me to this area. It was a pleasure to study with her.

I also want to thank to Can Özsoy, Cem Bingöl, and Koray Deniz Göral for enjoyable times that we shared. They always supported and directed me to do the best. I also want to thank to Emre Yıldırım and Mert Yaman for fruitiness time we shared and for their contribution to this study. I also want to extend my thanks to Aslıhan Devran, Berkay Akyol, Bora Yalçıner, Efekan Çevik, Emrecan Işık, Ghazal Khodkar, Gözde Güney Doğan Bingöl, Günay Gazaloğlu, İlker Çoban, Kadir Karakaş, Sedat Gözlet, Utku Uzun and Yağız Arda Çiçek for good memories.

I would like to thank to Ahmet Narman, Altuğ Oruç, Barış Yıldız, Başat Savrun, Bilgin Koçak, Burak Yolcu, İklim Okyar, Meriç Memiş, Mustafa Sayar, Şeyma Şahin, Uğur Şatır and Umut Şahin for their friendships and joyful times that we shared.

I would like to express my special thanks to Engin Durmuş, Gökay Yavuz, Alperen İnci, and Duhan Eşiyok for their friendships throughout my life.

I would like to express my special thanks to Ahmet Atacan, Eray Tuncan, Esat Fazlullah Çelik, Harun Yorgancıoğlu, Hilal Nur Çalık, Mehmet Sergen Çatal, Muhammed Alperen Özkan, Recep Sever, Sinan Ali Bilmez and Zeynep Denizmen for their friendship last a lifetime.

Finally, I want to express my deep gratitude to my mother, Emine Şentürk, my father, Fikret Şentürk, and my dearest friend, Pınar Ezgi Türközü, for their endless supports. They were always with me and supported me without any questions. I appreciate their trust in me. I feel fortunate to have such people.

TABLE OF CONTENTS

LIST OF TABLES

TABLES

LIST OF FIGURES

FIGURES

LIST OF ABBREVIATIONS

ABBREVIATIONS

CFD	Computational Fluid Dynamics
FAM	Finite Area Method
GCI	Grid Convergence Index
IBM	Immersed Boundary Method
MAPE	Mean Absolute Percentage Error
MULES	Multidimensional Universal Limiter with Explicit Solution
NRMSE	Normalized Root Mean Square Error
OpenFOAM	Open-source Field Operation and Manipulation
PISO	Pressure Implicit with Splitting Operator
RANS	Reynolds Averaged Navier Stokes
SIMPLE	Semi-Implicit Method for Pressure Linked Equations
SPH	Smoothed-Particle Hydrodynamics
VARANS	Volume Averaged Reynolds Averaged Navier Stokes
VOF	Volume of Fluid
WF	Wall Function
WG	Wave Gauge

LIST OF SYMBOLS

SYMBOLS

α	Linear friction coefficient
β	Non-linear friction coefficient
γ	VOF indicator function
δ	Kronecker delta
δ^+	Non-dimensional viscous sublayer thickness
ε	Turbulent dissipation
η	Free surface elevation
θ'	Shields parameter
θ'_c	Critical Shields parameter to initiate the motion
θ'_{c0}	Critical Shields parameter for a horizontal bed
λ_b	Linear concentration
μ_d	Dynamic friction coefficient
μ_s	Static friction coefficient
μ	Molecular dynamic viscosity
μ_l	Molecular dynamic viscosity of the liquid phase
μ_g	Molecular dynamic viscosity of the gas phase
μ_{eff}	Effective dynamic viscosity
ν_{turb}	Turbulent kinematic viscosity
ρ	Density

ρ_g	Density of the gas phase
ρ_l	Density of the liquid phase
ρ_s	Density of the sediment
τ_{ij}	Reynolds stress tensor
ϕ	Porosity
ω	Specific rate of dissipation
ω_{log}	Specific dissipation rate in the logarithmic region
ω_{vis}	Specific dissipation rate in the viscous sublayer
Ω_{ij}	Mean rotation rate
b	Reference level
c	Suspended sediment concentration
c_0	Maximum attainable volumetric concentration
c_b	Suspended sediment concentration at the reference level
C	Added mass coefficient
d	Water depth
D_{50}	Nominal mean grain diameter of the porous zone
D_s	Deposition due to the suspended sediment transport
E	Richardson error estimator
E_s	Erosion due to the suspended sediment transport
f	Face of the cell
f_f	Friction force

F_D	Combination of drag and lift forces
F_s	Factor of safety
g_i	Gravitational acceleration
h_b	Bed elevation
$h_{b,b}$	Bed level change due to the bed load transport
$h_{b,s}$	Bed level change due to the erosion and deposition
H	Wave height
i	Unit vector
k	Turbulent kinetic energy
K_s	Smooth wall coefficient
K_r	Rough wall coefficient
KC	Keulegan-Carpenter number
L	Length of the scour hole
p	Pressure
$\langle p \rangle^f$	Intrinsic pressure
P_b	Buoyancy production term
P_{EF}	Percentage of particles in motion in the surface layer of the bed
Q	Overtopping volume
q_b	Bed load transport rate
s	Specific gravity
S	Depth of the scour hole
S_{ij}	Mean-strain-rate tensor

t	Time
T_0	Period of the oscillation
u_i	Velocity
$\langle u_i \rangle$	Volume-averaged velocity
U_b	Mean transport velocity of the particle
U_f	Friction velocity
U_m	Maximum value of the velocity of oscillation
U_r	Velocity of flow relative to the particle
w_s	Settling velocity
W	Number of faces
W_τ	Gravitational force
x_i	Cartesian coordinate
X_s	Distance of the deepest point to the crown wall
y	Vertical distance from the wall
Δy	Vertical cell thickness of the first cell
Δy^+	Non-dimensional vertical cell thickness of the first cell

CHAPTER 1

INTRODUCTION

1.1 Motivation

Protecting the coastal areas from wave attacks is one of the significant purposes of coastal engineering applications. In this context, coastal protection structures have been constructed for decades to preserve these areas. Among the variety of these structures, each one is constructed for a particular purpose. Herein, coastal revetments are the sloped structures that are constructed to protect the coastal areas and roads by absorbing the incoming wave energy. There are several types of coastal revetments, and one of the most commonly used ones is the rubble mound coastal revetment. The rear side of this type of structure is generally filled with some materials such as sand, stone, grass, or asphalt. When there is a significant wave attack, the rear side of these structures might be damaged due to the overtopping of the waves and the impact of the jet flows. The extent of the damage at the rear side of the structure caused by the overtopping of waves has been widely investigated using experimental methods for several years. Yet, two recent experimental studies (Yildirim, 2021 and Yaman, 2022) investigated the scour of a non-cohesive bed material that is placed at the rear side of a coastal revetment under random and solitary wave attacks.

On the other hand, numerical tools are becoming more convenient and robust with the help of the developing advanced computer technologies. In this context, computational fluid dynamics (CFD) is a popular method in coastal engineering applications. There are several advantages of using CFD tools, such as easier and cheaper simulations. Furthermore, it provides to visualize any variable at any time and location, which is not possible for most experimental studies. In recent years,

CFD tools have been widely used to simulate several coastal engineering problems, and sediment transportation modeling is one of them (Baykal et al., 2015; Li et al., 2021). Even if most past studies concerning sediment transport and scour are generally based on laboratory experiments (Sumer et al., 2003; Yildirim, 2021; Yaman, 2022), using CFD tools is gaining popularity nowadays. On the other hand, besides their advantages, there are still some incomprehensible areas of using CFD tools that are open for further investigations. For example, high computational demand is one of the most challenging issues that users face. In large-scale simulations, small mesh sizes generally cannot be achieved due to the high computational demand. On the other hand, the Kolmogorov microscale, which is the smallest scale in a turbulent flow, should be used to capture the turbulence properties. However, it is usually not possible to generate the meshes in these scales. Therefore, turbulent properties cannot be captured accurately. As a result, accurate turbulence modeling is needed for a realistic simulation, particularly for scouring studies, since it is an essential parameter that affects the sediment transport rates, according to Sumer et al. (2003). In addition, using appropriate wall functions is a significant factor for a realistic scour simulation since the sediment transport is highly related to the near-wall behavior.

1.2 Objectives of the Study

This thesis study evaluates the performances of different turbulence models with wall functions to simulate the scour at the rear side of a rubble mound coastal revetment due to the overtopping of waves. During this study, solitary-like waves are studied to reduce the computational cost of the simulations. In the studies, a CFD toolbox called OpenFOAM is used to simulate the free surface and porous media flows. Both hydrodynamic and morphological numerical results are compared with the experimental results of Yaman (2022). This study is particularly focused on the following research questions:

i. What are the porous media friction coefficients for a solitary-like wave – rubble mound coastal revetment interaction?
ii. How do different turbulence model and wall function couplings affect the hydrodynamics results regarding free surface elevations, overtopping volumes, and jet thicknesses?
iii. What are the effects of using different turbulence model and wall function couplings on the morphological results regarding the scour profiles, depths, lengths, and the distance of the deepest point to the crown wall?
iv. Which turbulence model and wall function couple does show the best result in hydrodynamic and morphological studies?
v. Which sediment transportation process governs at the rear side of the coastal revetment?

This thesis study consists of two main stages: hydrodynamic and morphological studies. In the first part, a wave generation toolbox is used to generate the solitary-like waves with a free surface capturing methodology in addition to the porous media modeling. In the second part of the study, a sediment transport module is used to calculate the sediment transport rates. Then, the bottom elevation is changed using a mesh updating algorithm. All simulations are repeated for different turbulence model and wall function couplings to investigate the effect of turbulence.

1.3 Contents of the Chapters

In the second chapter, past studies related to this thesis study are given. First, the wave overtopping studies, the rear side damage studies, and the numerical studies of scouring due to the spillways, jets, and overflows are discussed. Then, the past studies related to computational fluid dynamics such as free surface capturing, wave generation and absorption, sediment transportation modeling, porous media modeling, turbulence modeling, and wall functions are summarized. Furthermore, gaps in the literature about the topic of this study are also discussed.

In the third chapter, the methodology of the study and the model descriptions are given. This chapter is mainly divided into two parts named hydrodynamic and morphological studies. In the first part, the CFD toolbox that is used in this study is described. Furthermore, the governing equations, porous media modeling, free surface capturing methodology, solution procedure, turbulence modeling, wall functions, wave generation, and absorption procedures are described in detail. Moreover, numerical model settings, including the computational domain, boundary conditions, and simulation properties, are given in the same part. In the second part, governing equations for morphological studies are presented. Then, the computational domain, truncated mesh, boundary conditions, and the wall functions are described. Finally, the properties of the simulations are given.

In the fourth chapter, simulation results are presented and discussed. This chapter consists of two main parts named hydrodynamic and morphological results. In the hydrodynamic results, the calibrated porous media coefficients are first given, and the free surface elevations are compared with the experimental results. Then, the overtopping volumes and the jet thicknesses are presented and compared with the experimental data. Furthermore, turbulent parameters are also shown to discuss the effects of different turbulence model and wall function couplings on the hydrodynamic simulations. In the morphological results, bed profiles and scour hole properties such as the scour depth, length, and the distance of the deepest point to the crown wall are presented and compared with the experimental data. Furthermore, these results are discussed in the light of turbulent parameter results to investigate the performances of turbulence model and wall function couplings on morphological studies. Finally, non-dimensional wall shear stress (Shields parameter) values are presented and discussed to understand the governing sediment transportation process at the rear side of the coastal revetment.

In the fifth chapter, a summary of this study, including the simulation results and the findings, are given. Moreover, further recommendations and possible future studies to extend this thesis study are presented.

CHAPTER 2

LITERATURE REVIEW

Seas and coastal areas are very vulnerable environments to human impacts; therefore, it is needed to consider the possible outcomes of constructing the coastal structures. After the construction of a facility in such an environment, the flow properties change, and several new ones such as vortex regimes, flow separations, pressure changes, differentiation in turbulence, etc., can be observed, which may result in scouring of the bed material (Sumer et al., 2001). Scour at the rear side of a rubble mound coastal revetment caused by the overtopping of waves is an example of such a process, and this is also the primary concern of this study. Various numerical and physical research has been done in the literature to investigate this topic. In the first part of this chapter, numerical and physical studies of scouring at the rear side of the coastal revetments are given. Then, computational fluid dynamic tools and the properties of the numerical models are presented in the second part.

2.1 Scour at the Rear Side of a Rubble Mound Coastal Revetment

As the first step of this study, overtopping discharges due to short crested waves and solitary waves are considered. The most comprehensive physical studies for overtopping discharges for different structure types and flow properties are collected in EurOtop (2018). Moreover, one of the most extensive experimental wave overtopping databases for coastal structures is collected under the CLASH project with the contribution of several universities to develop a neural network tool for the prediction of wave overtopping (Meer et al., 2009). Furthermore, various numerical studies in the literature are studied to determine the wave overtopping discharge

volumes using different models. Dodd (1998) and Hu et al. (2000) studied wave overtopping using one-dimensional numerical models that solve the non-linear shallow water equations. Then, Hubbard and Dodd (2002) further developed the previously mentioned one-dimensional model to a two-dimensional model and studied wave run-up and overtopping. Later, Losada et al. (2008) studied the wave overtopping of rubble mound breakwaters using a two-dimensional numerical model, COBRAS-UC, which solves Volume Averaged Reynolds Averaged Navier-Stokes (VARANS) equations with a free surface capturing method. Hsiao and Lin (2010) studied the overtopping of tsunami-like solitary waves using COBRAS which solves Reynolds Averaged Navier-Stokes (RANS) equations combined with a k-ε turbulence model and a free surface capturing method. After developing several numerical models, a comparison of three different ones (SWASH which solves non-hydrostatic non-linear shallow water equations, DualSPHysics, and FLOW-3D, which solve Navier-Stokes Equations) to determine the overtopping performances on a sea wall is discussed by Vanneste et al. (2014). Recently, Chen et al. (2021) studied wave overtopping at dikes by solving VARANS equations with a free surface capturing method in OpenFOAM environment and investigated the effects of the berm and protruding blocks on overtopping discharges. To conclude, several numerical studies have been studied in the literature and validated by physical model experiments. These studies showed that wave overtopping could be predicted accurately using numerical models.

As the second step of this study, the effects of wave overtopping at the rear side of the coastal revetments are considered. Schmocker and Hager (2010) studied the dike breaches due to the overtopping of waves considering trapezoidal cross-sections. Then, Steendam et al. (2014) studied the effects of transition between hard and soft layers and the obstacles at the rear side of dikes to the erosion of the grass layer. Later, Bomers et al. (2018) used a hydrodynamic-erosion model to investigate the effect of an asphalt road at the top of a dike on the erosion on the grass layer due to the overtopping of waves. Furthermore, Warmink et al. (2018) studied the transition effect on grass layers on dike erosion. For the rear side design purposes, Gent and

Pozueta (2005) and Gent (2007) are determined the rear side stone sizes and the expected damages for rubble mound structures without and with crest elements, respectively. Recently, Yildirim (2021) studied the erosion at the rear side of a coastal revetment caused by the overtopping of waves. Furthermore, this study investigated the relation between scour depths and the overtopped discharge volumes experimentally. To conclude, there are several studies about the effect of overtopping discharges at the rear side of the structures, yet, most of these are physical studies, which shows a gap in the literature about the numerical studies of the topic.

As the final step of this study, scour processes due to the spillways, jets, and overflows are considered since the phenomenon of these studies is analogous to the scour at the rear side of a coastal revetment. Neyshabouri et al. (2003) studied the numerical simulation of scouring due to a free-falling jet. In the first step, the free-falling jet is simulated using the k-ε turbulence model. Then, the concentration of the erodible material is computed to determine the bed topology. Amiraslani et al. (2010) studied the same topic with a 3-D model in FLOW-3D environment. Furthermore, Castillo et al. (2012) and Movahedi et al. (2017) studied the numerical simulations of scouring the downstream of a dam using FLOW-3D. For tsunami overflow cases, Tsujimoto et al. (2014) studied a dam break simulation due to its similarity to tsunami overflow. Numerical and experimental values of velocity and turbulent kinetic energy in the scour hole are compared using a model called CADMAS-SURF. Furthermore, Jayaratne et al. (2014) developed a predictive model to determine the scour depths due to tsunami overflows. Large Eddy Simulations (LES) have been carried numerically to determine the pressure values due to the overflow and velocity values of the inundation. To conclude, there are several analogous studies in the literature, yet, a numerical analysis of scouring at the rear side of a coastal revetment caused by the overtopping of waves is a gap in the literature.

2.2 Computational Fluid Dynamics (CFD)

CFD tools are among the most up-to-date topics in the engineering area; besides, CFD markets are growing approximately %15 each year (Ferziger et al. 2020). With the help of the latest models, computational fluid dynamics tools are capable of reflecting reality in many ways. Some of these are capturing and tracking the free surface, wave generation and absorption, sediment transport modeling, porous media modeling, turbulence modeling, and the application of wall functions within the turbulence modeling framework. In the following sections, past studies about these topics are discussed.

2.2.1 Free Surface Capturing and Tracking

In most CFD applications (Jacobsen et al., 2012; Higuera et al., 2013; Guler et al., 2018), the free surface is captured using two-phase flow models. Mirjalili et al. (2017) divided the two-phase flow models into four categories which are Lattice Boltzmann Method (LBM), Smoothed-Particle Hydrodynamics (SPH), Two-Fluid Models, and One Fluid Models. The study's main concern was the one-fluid models, which are categorized as Volume of Fluid Method (VOF), Level Set Method, and Phase Field Method. In VOF, volume fraction values at each cell are determined, and the free surface is captured using these fractions. The first study about VOF is by Hirt and Nichols (1981), where the technique is established to determine the complicated free surfaces for incompressible flows. Then, Deshpande et al. (2012) studied the performance of *interFoam*, which is a multiphase flow solver using VOF with MULES solver (Multidimensional Universal Limiter with Explicit Solver) in OpenFOAM CFD library. Later, Roenby et al. (2016) developed a novel method for VOF called *isoAdvector*, which shows more accurate results than MULES in general. Recently, Larsen et al. (2019) evaluated the performance of *interFoam* to simulate the progressive waves by considering the effects of discretization schemes, solver settings, temporal and spatial resolutions. Furthermore, VOF is successfully applied

to several coastal engineering studies in the literature, and the results agreed well with the experimental studies (Arikawa et al., 2011; Jesus et al., 2012; Higuera et al., 2014a; Guler et al., 2018). As a result, the past studies in the literature show that VOF can be applied to free surface capturing problems to produce accurate results.

2.2.2 Wave Generation and Absorption

Realistic wave generation and absorption in three-dimensional Navier-Stokes equations are needed for coastal engineering applications to reflect the reality in the simulations. Jacobsen et al. (2012) developed *waves2Foam*, which is a toolbox to generate and absorb the waves solving RANS equations with VOF using OpenFOAM CFD library. In the study of Jacobsen et al. (2012), wave absorption is done using relaxation zones which can avoid the reflection of the waves at the wave generating inlet boundaries and the outlet boundaries. Then, Higuera et al. (2013) developed wave generation and absorption boundary conditions based on OpenFOAM CFD library. In this study, Stokes I-II (Dean and Dalrymple, 1991), Stokes V (Skjelbreia and Hendrickson, 1960), Cnoidal (Svendsen, 2006), Streamfunction (Fenton, 1988), and Solitary (Lee et al., 1982) wave theories are used to generate waves. Furthermore, active wave absorption is used instead of relaxation zones. In the active wave absorption method, the reflected waves are avoided by producing a velocity profile in the opposite direction at the boundaries. Therefore, the computational demand is generally decreased compared to the passive wave absorption method since there is no need to define an additional relaxation zone. In the literature, numerical wave generation and absorption simulations are done successfully in several coastal engineering-related studies (Jacobsen, 2011; Guler, 2020; Chen et al., 2021). To conclude, the studies in the literature show that wave generation and absorption can be modeled accurately using numerical tools.

2.2.3 Sediment Transport Modeling

One of the earliest studies on the mathematical description of sediment transport was done by Einstein (1950), where the bed load transport equations are developed by considering the force balance equations using a statistical approach. Furthermore, Einstein (1950) described the bed load with two non-dimensional parameters (non-dimensional forms of the transport rate and the tractive stress). Then, Engelund and Fredsoe (1976) discussed and further developed the findings of the previous studies to determine more extensive bed load and suspended load equations. One of the most comprehensive studies is done by Fredsoe and Deigaard (1992), where the coastal sediment transport phenomenon and the hydrodynamic processes behind it are explained in detail. Roulund et al. (2005) can be considered as a milestone of three-dimensional numerical studies of sediment transport. In this study, 3D RANS equations are solved with k-ω SST turbulence closure in EllipSys3D Model using a finite volume method. The model is coupled with a sediment transport module, where the study of Engelund and Fredsoe (1976) is further extended, and sand slide phenomena are also considered. The model can also evaluate the bed elevation using a sand continuity equation. It should also be noted that suspended load contribution is not considered in Roulund et al. (2005). Then, Fuhrman et al. (2013) studied the sediment transport rates under sheet flow conditions using a 1D model (MatRANS). In this study, hindered settling velocities and the turbulent suppression terms are also considered, but the morphological change is not studied. The study done by Fuhrman et al. (2013) is then extended in Caliskan and Fuhrman (2017) by considering the graded sediments under sheet flow conditions. Then, a fully coupled hydrodynamic-morphological model is developed by Jacobsen (2011) in the OpenFOAM CFD library. The model solves 3D RANS equations with user-defined turbulence closures in addition to sediment transport equations (bed load, suspended load, and sand slide) coupled with a mesh update algorithm to consider the bed morphology changes. The model has been used in several studies. Jacobsen et al. (2014) used it to study the development of breaker bar indexes for regular waves.

Furthermore, Baykal et al. (2014) studied the backfilling processes around vertical piles. Then, the numerical simulations of flow, scour, and backfilling are studied by Baykal et al. (2017). As a recent study, Li et al. (2021) used the same model to simulate the scour around a vertical pile placed on a sloping bed under wave attack. Studies that are presented above show that the bed load and suspended load approach can be used for realistic sediment transport simulations.

There are also other approaches to solve the sediment transport phenomenon in the literature. Cheng et al. (2017) presented s*edFoam*, which is an Eulerian two-phase model based on the OpenFOAM CFD library, so it does not consider bed load and suspended load contributions. Furthermore, Sun and Xiao (2016) presented *sediFoam*, which is a CFD-DEM (Computational Fluid Dynamics – Discrete Element Method) coupled model, so it does not need to consider the sediment transport equations. However, as Sun and Xiao (2016) reported, the model is not suitable for large-scale simulations due to its high computational time.

2.2.4 Porous Media Modeling

Modeling the porous media can be achieved using two different approaches named microscopic and macroscopic approaches. Because the time cost of the microscopic approach is very high and accurate mesh generation is challenging, it is difficult to be used for coastal engineering problems (Losada et al. (2016)). On the other hand, the overall behavior of the flow inside the porous media can be determined using the macroscopic approach, which is also used in this thesis study. The Forchheimer equation can be considered as a milestone for porous media modeling, and Whitaker (1996) reviewed its theoretical development. Furthermore, Gent (1995) studied the porous media effects on Navier-Stokes equations. Then, Jesus et al. (2012) studied the wave-porous media interactions using volume averaging techniques inside the porous media. In the study of Jesus et al. (2012), Volume Averaged Reynolds Averaged Navier-Stokes (VARANS) equations are closed using the extended Darcy-Forchheimer equation. Next, Jensen et al. (2014) reviewed and further developed the

porous media equations and determined the ideal resistance coefficients. Furthermore, Higuera et al. (2014a) implemented the porous media equations in the OpenFOAM CFD library and validated them against experimental data for wave–porous structure interactions. As a recent study, Guler (2020) presented *ibmPorFoam*, which uses body force Immersed Boundary Method (IBM) for static meshes with porous media equations in the OpenFOAM CFD library. Furthermore, *rubbleFoam*, which uses cut-cell IBM for moving boundaries with porous media modeling, is also developed in the same study. Studies in the literature show that the macroscopic approach of porous media modeling can be successfully applied to coastal engineering problems.

2.2.5 Turbulence Modeling

Like most other physical phenomena, the primary source of the perception of turbulence is observation. In this context, artists, as good observers, are the ones who have first realized the turbulence. According to Marusic and Broomhall (2021), in the writings of Leonardo da Vinci, the word "*turbolenza*" is used several times. Furthermore, it is a well-known fact that Vincent van Gogh used turbulence in his paintings (Beattie and Kriel, 2019)

As Rodi (2017) states, most fluid flows are turbulent, and Reynolds Numbers are high, resulting in significant changes in the momentum transport. Turbulence is, in fact, a well-known topic since the 1800s, and Rodi (2017) presented a historical development of turbulent models from the 1800s to the present. Sumer et al. (2003) also showed the importance of externally generated turbulence on bed load transport and scouring rates. One of the most comprehensive studies about turbulence modeling for CFD applications is Wilcox (2006) which explains the physics and mathematics behind the phenomenon. To simulate the scour and backfilling processes around a vertical pile, Baykal et al. (2017) used the two-equation k-ω turbulence closure explained by Wilcox (2006) and Wilcox (2008). Furthermore, Fuhrman et al. (2013) used a modified form of the same turbulence model by

considering the turbulent suppression terms to calculate the sediment transport rates. As a recent study, Larsen and Fuhrman (2018) solved the overproduction problem of the turbulent models beneath the surface waves using a methodology briefly explained by Mayer and Madsen (2001). As it is shown, various turbulence models were presented in the literature. Each one shows different characteristics, so choosing the appropriate turbulence model is left to the user's preference. On the other hand, Sumer et al. (2003) showed that turbulence significantly affects the sediment transport rates. Therefore, selecting the proper turbulence model is essential for the sediment transport simulations. Although different turbulence models are developed and used for morphological studies, there is not a comprehensive evaluation of the performances of the turbulence models for simulating the scour. The equations solved by two-equation turbulence models are elaborated in Chapter 3.

2.2.6 Wall Functions

As Kalitzin et al. (2005) stated, well-defined wall functions are needed for accurate CFD modeling since the mesh sizes are generally not enough for a wall integration. An early and comprehensive study about the near-wall region flow characteristics is Spalding (1961) which compares the wall functions developed by Prandtl (1910), Taylor (1916), Karman (1939), Reichardt (1951), Deissler (1955), Driest (1956) and Rannie (1956). Furthermore, in Spalding (1961), a single experimental formula is fitted to the near-wall region such that it can be used for the viscous sublayer, buffer region, and turbulent region. Later, Shih et al. (1999) developed a generalized wall function that can show a good approximation for the flows having adverse pressure gradients. Next, Nichols and Nelson (2004) derived a wall function that can consider the effects of heat transfer and compressibility. One of the main developments about the wall functions is discovered by Saffman (1970), which recognizes that the surface roughness effects can be included using a specific rate of dissipation (ω) boundary condition. One of the most comprehensive studies about the wall functions

and turbulence modeling is Wilcox (2006), which explains both the phenomenon's physics and mathematics. Recently, Fuhrman et al. (2010) compared the Neumann and Dirichlet boundary conditions applied to the turbulent kinetic energy (k) using a k-ω model in addition to the wall functions explained by Wilcox (2006). In the study, turbulent parameters are compared with the experimental data. Later, wall functions by Fuhrman et al. (2014) are used to study the scour under the submarine pipelines. In the study, it is also noted that the given wall functions show a good agreement with the experimental data by Fuhrman et al. (2010). As it is explained, there are several wall functions in the literature. According to Liu (2016), using an appropriate wall function is significant to capture the physics of the turbulence in the near-wall region. Since the scour processes generally occur close to the wall, it is essential to use the proper wall functions to compute the accurate turbulence properties in that region. Although the wall functions are developed and used several times in the literature, the different wall functions' performances to the scour profiles are still unclear.

CHAPTER 3

DESCRIPTION OF THE NUMERICAL MODEL

In this study, scour at the rear side of a rubble mound coastal revetment is simulated numerically to investigate the effects of turbulence models and wall functions on morphology changes. This section consists of two parts. In the first part, the hydrodynamic model is described. Furthermore, methodologies for free surface capturing, wave generation and absorption, porous media modeling, turbulence modeling, and wall function applications are explained. In the second part, the morphological model, including the methodologies for the bed load and suspended load transports, sand slide phenomena, and the morphological update routine, is described.

3.1 Hydrodynamics Model

3.1.1 Model Description and Governing Equations

In this study, a commonly used computational fluid dynamics (CFD) tool, OpenFOAM (Open-source Field Operation and Manipulation), is used. OpenFOAM is a toolbox developed with C++, enabling users to manipulate and further develop the source codes. There are several OpenFOAM distributions such as FOAM-Extend by Wikki Ltd., OpenFOAM by ESI Group, and OpenFOAM Foundation Inc. by OpenFOAM Foundation Ltd. Throughout this study, FOAM-Extend-1.6 distribution is used since the source code of the morphological model is written in the FOAM-Extend-1.6 environment.

The OpenFOAM environment provides users to solve Navier-Stokes equations and the variants using the Finite Volume Method (FVM). Users can also generate proper computational domains and choose the appropriate boundary conditions,

discretization schemes, solutions algorithms, turbulence models, and other settings. It is also capable of solving several complex phenomena such as multiphase problems, moving boundary problems, compressible and incompressible flows, heat transfer, etc.

One of the main advantages of OpenFOAM is that users can implement and use the solvers, turbulence models, and packages developed by other users. In this study, a solver called *ihFoam* developed by Higuera et al. (2014a) is used to consider the porous media effects inside the rubble mound coastal revetment.

ihFoam is a three-dimensional two-phase flow solver that can consider the porous media effects by solving Volume Averaged Reynolds Averaged Navier-Stokes (VARANS) equations inside the porous media. Furthermore, it is based on *interFoam*, which is a three-dimensional two-phase flow solver that solves Reynolds Averaged Navier-Stokes (RANS) equations. Therefore, when a porous media is presented, *ihFoam* solves VARANS equations. On the other hand, if porosity is not defined, it solves RANS equations in the same way with to *interFoam*.

3.1.1.1 RANS Equations

Due to its high computational power demand, solving the conventional form of Navier-Stokes equations with a proper mesh is not easy in most cases. Therefore, these equations are averaged using Reynolds-averaging methods, and the final closed form of these equations is called Reynolds Averaged Navier-Stokes (RANS) equations. A detailed procedure for Reynolds averaging is given by Ferziger et al. (2020). The continuity and momentum equations of RANS, which are solved by the *ihFoam* solver in the absence of porous media in the computational domain, are given in (3.1) and (3.2), respectively.

$$\frac{\partial u_i}{\partial x_i} = 0 \tag{3.1}$$

$$\frac{\partial \rho u_i}{\partial t} + u_j \frac{\partial \rho u_i}{\partial x_j} = -\frac{\partial p}{\partial x_i} + \rho g_i + \frac{\partial}{\partial x_j}\left(\mu_{eff} \frac{\partial u_i}{\partial x_j}\right) \quad (3.2)$$

Here, u_i is the ensemble-averaged velocity, x_i is the Cartesian coordinate, p is the pressure, t is time, g_i is the gravitational acceleration, ρ is the density and μ_{eff} is the effective dynamic viscosity, which can be computed as $\mu_{eff} = \mu + \rho \nu_{turb}$, where μ is the molecular dynamic viscosity and ν_{turb} is the turbulent kinematic viscosity which can be determined using the turbulence models accordingly.

3.1.1.2 Porous Media Modeling: VARANS Equations

A volume averaging methodology described by Whitaker (1999) is applied to RANS equations to consider the flow through a porous zone. After the volume averaging, the terms that appear due to the nature of the averaging methodology cannot be solved directly and must be modeled. An extended Darcy-Forchheimer equation is applied to close the equation, and VARANS equations are obtained. A detailed theoretical development is given by Jensen et al. (2014). In the literature, various closure parameters have been described, and one of the most comprehensive studies is given by Gent (1995). Later, Higuera et al. (2014a) modified the VARANS equations and the closure parameters described by Gent (1995) to be solved in an OpenFOAM environment. The continuity and momentum equations of VARANS, which are solved by the *ihFoam* solver inside the porous zone, are given in (3.3) and (3.4).

$$\frac{\partial \langle u_i \rangle}{\partial x_i} = 0 \quad (3.3)$$

$$\frac{1+C}{\phi}\frac{\partial \rho\langle u_i\rangle}{\partial t}+\frac{1}{\phi}\frac{\partial}{\partial x_j}\left[\frac{\rho\langle u_i\rangle\langle u_j\rangle}{\phi}\right] = -\frac{\partial\langle p\rangle^f}{\partial x_i}+\rho g_i+\frac{1}{\phi}\frac{\partial}{\partial x_j}\left(\mu_{eff}\frac{\partial\langle u_i\rangle}{\partial x_j}\right) - \alpha\frac{(1-\phi)^3}{\phi^3}\frac{\mu}{D_{50}^2}\langle u_i\rangle - \beta\left(1+\frac{7.5}{KC}\right)\frac{(1-\phi)}{\phi^3}\frac{\rho}{D_{50}}\sqrt{\langle u_j\rangle\langle u_i\rangle}\langle u_i\rangle \tag{3.4}$$

Here, $\langle u_i\rangle$ is the volume-averaged velocity, x_i is the Cartesian coordinate, $\langle p\rangle^f$ is the intrinsic pressure, t is time, g_i is the gravity, ρ is the density and μ_{eff} is the effective dynamic viscosity which can be computed as $\mu_{eff}=\mu+\rho\nu_{turb}$, where μ is the molecular dynamic viscosity and ν_{turb} is the turbulent kinematic viscosity which can be determined using the turbulence model accordingly.

The other parameters are the closure parameters that appeared after the volume averaging to close the equation. ϕ is the porosity, D_{50} is the nominal mean grain diameter of the porous zone, KC is the Keulegan-Carpenter number defined as $KC=\frac{T_0}{D_{50}}\frac{U_m}{\phi}$ where T_0 is the period and U_m is the maximum value of the velocity of oscillation. Although there are several other variants (Losada et al., 2016) of the last two terms of the right-hand side of (3.4), these are the ones that are presented by Higuera (2015). In these terms, α and β are the friction coefficients that should be calibrated accordingly. In this study, they are calibrated using the experimental results to obtain realistic simulations in morphological studies. Finally, C is the added mass coefficient, and it is suggested to be taken as 0.34 by Jesus et al. (2012).

3.1.1.3 Free Surface Modeling: Volume of Fluid (VOF) Method

In most coastal engineering problems, the free surface has great importance, and it should be captured accurately. In both *interFoam* and *ihFoam* solvers, the VOF method is used to capture it. In this method, an indicator function (γ) is used to identify the fluid phases such that it is equal to 1 if the fluid in the computational cell

is fully liquid, and it is equal to 0 if the cell is full of gas. Once γ values of each cell are determined, any physical properties can be weighted and modified. Fluid density and the molecular viscosity of each cell can be modified using (3.5) and (3.6).

$$\rho = \gamma\rho_l + (1-\gamma)\rho_g \tag{3.5}$$

$$\mu = \gamma\mu_l + (1-\gamma)\mu_g \tag{3.6}$$

Here, ρ_l and μ_l are the density and molecular viscosity of the liquid phase, respectively. On the other hand, ρ_g and μ_g are the ones for the gas phase.

To determine γ values, an advection equation is solved by OpenFOAM. The volume-averaged VOF-advection equation (Higuera, 2015) that *ihFoam* solves is given by (3.7). The last term in (3.7) is included to consider the compression of the interface between the phases based on the discussions given by Berberovic et al. (2009).

$$\frac{\partial\gamma}{\partial t} + \frac{1}{\phi}\frac{\partial\gamma\langle u_i\rangle}{\partial x_i} + \frac{1}{\phi}\frac{\partial\gamma(1-\gamma)\langle u_i\rangle}{\partial x_i} = 0 \tag{3.7}$$

3.1.1.4 Solution Procedure and Algorithms

In the OpenFOAM environment, differential equations are solved using the appropriate solvers and algorithms. In both *interFoam* and *ihFoam*, the VOF-advection equation (3.7) is solved using the Multidimensional Universal Limiter with Explicit Solution (MULES) module, which introduces a limiter to bound γ in between 0 and 1. After determining γ, the physical properties are updated using (3.5) and (3.6). Further information about MULES and the discretization schemes is given by Deshpande et al. (2012).

ihFoam uses the PIMPLE algorithm, which is a combination of PISO (Pressure Implicit with Splitting of Operator) and SIMPLE (Semi-Implicit Method for Pressure Linked Equations) algorithms to solve the momentum equations (both RANS and VARANS). The structure of the algorithm is presented in Figure 3.1.

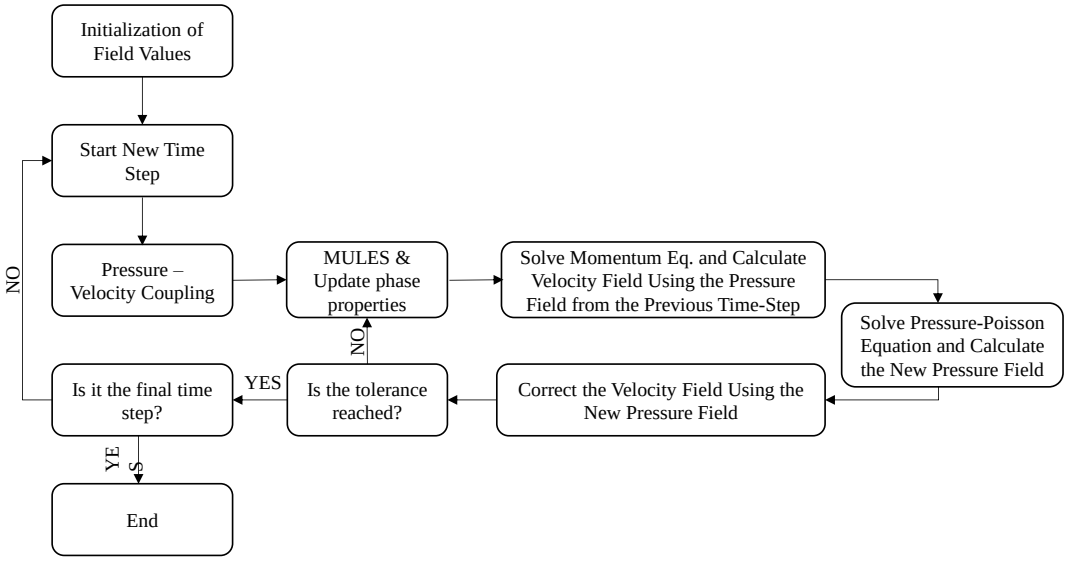

Figure 3.1: Structure of PIMPLE algorithm

As shown in Figure 3.1, first, the field values and the numerical setup (time step, tolerance, Courant Number, porosity, etc.) are initialized. Then, the related time step computations are started, and VARANS equations are solved in the pressure–velocity coupling loop. In this loop, first, the VOF-advection equation (3.7) is solved using MULES, followed by updating the phase properties. Next, the discretized form of the momentum equation is solved using the pressure field from the previous time step to calculate the velocity field. Then, the Pressure-Poisson Equation is solved using the velocity field to determine the new pressure field which is, then used to determine the new velocity field. In the final step of this loop, the error is calculated and compared with the tolerance. This process is repeated until the desired level of accuracy is satisfied, followed by the next time step. Furthermore, it should be noted that the continuity equation is solved to check whether the continuity is satisfied or not instead of computing the field values.

3.1.1.5 Turbulence Closure

Turbulence is an important phenomenon for most coastal engineering problems since it severely affects both flow characteristics and sediment transport rates. In both

RANS and VARANS equations, ν_{turb} should be calculated according to the user-defined turbulence model to determine μ_{eff}. In this study, simulations are carried on with five different turbulence models in addition to a laminar simulation. It is noted that the effective dynamic viscosity is equal to the molecular dynamic viscosity in the laminar simulations. Turbulence models are chosen as standard k-ε turbulence model (Launder and Sharma, 1974), standard k-ω turbulence model (Wilcox, 1988), k-ω turbulence model (Wilcox, 2006), k-ω SST turbulence model (Menter et al., 2003), and stabilized k-ω SST turbulence model (Larsen and Fuhrman, 2018). In all turbulence models, the recommended coefficients are used. These models are described in the following paragraphs.

k-ε Turbulence Model (Launder and Sharma, 1974)

k-ε turbulence model is one of the most commonly used two-equation models for CFD applications. In this study, the standard k-ε turbulence model is used. It was first presented by Launder and Sharma (1974), and it solves two partial differential equations related to the turbulent kinetic energy (k) and rate of dissipation of turbulent kinetic energy (ε). After determining these two unknowns, the turbulent viscosity (ν_{turb}) can be determined. The model equations are given in (3.8) and (3.9).

$$\frac{\partial k}{\partial t} + u_j \frac{\partial k}{\partial x_j} = \frac{\partial}{\partial x_j}\left[\left(\nu + \frac{\nu_{turb}}{\sigma_k}\right)\frac{\partial k}{\partial x_j}\right] + \tau_{ij}\frac{\partial u_i}{\partial x_j} - \varepsilon \tag{3.8}$$

$$\frac{\partial \varepsilon}{\partial t} + u_j \frac{\partial \varepsilon}{\partial x_j} = C_{\varepsilon 1}\frac{\varepsilon}{k}\tau_{ij}\frac{\partial u_i}{\partial x_j} - C_{\varepsilon 2}\frac{\varepsilon^2}{k} + \frac{\partial}{\partial x_j}\left[\left(\nu + \frac{\nu_{turb}}{\sigma_\varepsilon}\right)\frac{\partial \varepsilon}{\partial x_j}\right] \tag{3.9}$$

Here, the turbulent viscosity (ν_{turb}) can be determined as $\nu_{turb} = C_\mu k^2/\varepsilon$. Furthermore, the other coefficients used in the k-ε turbulence model are as follows: $C_{\varepsilon 1} = 1.44$, $C_{\varepsilon 2} = 1.92$, $C_\mu = 0.09$, $\sigma_k = 1.0$, $\sigma_\varepsilon = 1.3$.

Standard k-ω Turbulence Model (Wilcox, 1988)

k-ω turbulence model is one of the most widely used two-equation models to predict the eddy viscosity. It was first developed by Wilcox (1988), and it solves two partial differential equations related to the turbulent kinetic energy (k) and the specific rate of dissipation (ω) of the turbulent kinetic energy into internal thermal energy. After determining these two unknowns, the turbulent viscosity (ν_{turb}) can be determined as $\nu_{turb} = k/\omega$. The equations of the model are given below.

$$\frac{\partial \rho k}{\partial t} + \frac{\partial \rho u_j k}{\partial x_j} = \tau_{ij}\frac{\partial u_i}{\partial x_j} - \rho\beta^* k\omega + \frac{\partial}{\partial x_j}\left[(\mu + \rho\sigma^* \nu_{turb})\frac{\partial k}{\partial x_j}\right] \quad (3.10)$$

$$\frac{\partial \rho \omega}{\partial t} + \frac{\partial \rho u_j \omega}{\partial x_j} = \alpha\frac{\omega}{k}\tau_{ij}\frac{\partial u_i}{\partial x_j} - \rho\beta\omega^2 + \frac{\partial}{\partial x_j}\left[(\mu + \rho\sigma\nu_{turb})\frac{\partial \omega}{\partial x_j}\right] \quad (3.11)$$

Here, τ_{ij} is the Reynolds stress tensor, which is a well-known Boussinesq approximation and can be computed solving (3.12).

$$\tau_{ij} = 2\rho\nu_{turb}S_{ij} - \frac{2}{3}k\delta_{ij} \quad (3.12)$$

Moreover, in (3.12), S_{ij} is the mean-strain-rate tensor, which can be determined by solving (3.13).

$$S_{ij} = \frac{1}{2}\left(\frac{\partial u_i}{\partial x_j} + \frac{\partial u_j}{\partial x_i}\right) \quad (3.13)$$

Furthermore, the coefficients related to the model are given as follows: $\beta = 3/40$, $\beta^* = 9/100$, $\alpha = 5/9$, $\sigma = 1/2$, $\sigma^* = 1/2$.

k-ω Turbulence Model (Wilcox, 2006)

The k-ω turbulence model (Wilcox, 2006) is a further developed version of the standard k-ω turbulence model by Wilcox (1988). Apart from the standard model, this one includes the cross-diffusion term and a built-in stress limiter. According to

Baykal et al. (2017), this model is as accurate as of the other k-ω models while the closure coefficients are fewer. The model equations are given in (3.14) and (3.15). It should be noted that the equation for k (3.14) is analogous to (3.10), yet, it is written again for consistency.

$$\frac{\partial k}{\partial t} + u_j \frac{\partial k}{\partial x_j} = \frac{\tau_{ij}}{\rho}\frac{\partial u_i}{\partial x_j} - \beta^* k\omega + \frac{\partial}{\partial x_j}\left[\left(\nu + \sigma^* \frac{k}{\omega}\right)\frac{\partial k}{\partial x_j}\right] \tag{3.14}$$

$$\begin{aligned}\frac{\partial \omega}{\partial t} + u_j \frac{\partial \omega}{\partial x_j} &= \alpha \frac{\omega}{k}\frac{\tau_{ij}}{\rho}\frac{\partial u_i}{\partial x_j} - \beta\omega^2 + \frac{\sigma_d}{\omega}\frac{\partial k}{\partial x_j}\frac{\partial \omega}{\partial x_j} \\ &+ \frac{\partial}{\partial x_j}\left[\left(\nu + \sigma\frac{k}{\omega}\right)\frac{\partial \omega}{\partial x_j}\right]\end{aligned} \tag{3.15}$$

$$\sigma_d = H\left\{\frac{\partial k}{\partial x_j}\frac{\partial \omega}{\partial x_j}\right\}\sigma_{d0} \tag{3.16}$$

Here, H is the Heaviside step function. Moreover, the coefficients of this model are given as follows: $\beta = \beta_0 f_\beta$, $\beta_0 = 0.0708$, $\beta^* = 9/100$, $\alpha = 13/25$, $\sigma = 1/2$, $\sigma^* = 3/5$, $\sigma_{d0} = 1/8$ where f_β can be determined using (3.17).

$$f_\beta = \frac{1 + 85X_\omega}{1 + 100X_\omega}, \qquad X_\omega = \left|\frac{\Omega_{ij}\Omega_{jk}S_{ki}}{(\beta^*\omega)^2}\right|, \qquad \Omega_{ij} = \frac{1}{2}\left(\frac{\partial u_i}{\partial x_j} - \frac{\partial u_j}{\partial x_i}\right) \tag{3.17}$$

Finally, the turbulent eddy viscosity (ν_{turb}) can be determined as $\nu_{turb} = k/\tilde{\omega}$ where $\tilde{\omega}$ can be computed using (3.18).

$$\tilde{\omega} = max\left\{\omega, C_{lim}\sqrt{\frac{2S_{ij}S_{ij}}{\beta^*}}\right\} \tag{3.18}$$

Here, C_{lim} is taken as 7/8.

k-ω SST Turbulence Model (Menter et al., 2003)

k-ω SST (Shear Stress Transport) turbulence model is first developed by Menter (1993) to capture the main characteristics of the boundary layer. Then, the model is further developed by Menter et al. (2003). It can be described as a combination of k-ω and k-ε turbulence models such that k-ω turbulence model is activated near the

wall regions while the k-ε turbulence model is activated for the rest. The equations of the k-ω SST model are given below.

$$\frac{\partial \rho k}{\partial t} + \frac{\partial \left(\rho u_j k\right)}{\partial x_j} = \widetilde{P_k} - \rho \beta^* k\omega + \frac{\partial}{\partial x_j}\left[\left(\mu + \rho \sigma_k \nu_{turb}\right)\frac{\partial k}{\partial x_j}\right] \tag{3.19}$$

$$\frac{\partial \rho \omega}{\partial t} + \frac{\partial \left(\rho u_j \omega\right)}{\partial x_j} = \alpha \rho S^2 - \rho \beta \omega^2 + \frac{\partial}{\partial x_j}\left[\left(\mu + \rho \sigma_\omega \nu_{turb}\right)\frac{\partial \omega}{\partial x_j}\right] + 2(1 - F_1)\rho \sigma_{\omega 2}\frac{1}{\omega}\frac{\partial k}{\partial x_j}\frac{\partial \omega}{\partial x_j} \tag{3.20}$$

Here, F_1 is the blending function that activates the k-ω turbulence model inside the boundary layer and the k-ε turbulence model for the rest. It can be computed using (3.21).

$$F_1 = \tanh\left\{\left\{min\left[max\left(\frac{\sqrt{k}}{\beta^* \omega y}, \frac{500\nu}{y^2 \omega}\right), \frac{4\rho \sigma_{\omega 2} k}{CD_{k\omega} y^2}\right]\right\}^4\right\} \tag{3.21}$$

In (3.21), $CD_{k\omega}$ is the cross-diffusion term that can be determined using (3.22).

$$CD_{k\omega} = max\left(2\rho\, \sigma_{\omega 2}\frac{1}{\omega}\frac{\partial k}{\partial x_j}\frac{\partial \omega}{\partial x_j}, 10^{-10}\right) \tag{3.22}$$

In the k-ω SST turbulence model, the turbulent eddy viscosity (ν_{turb}) can be determined using (3.23).

$$\nu_{turb} = \frac{\alpha_1 k}{max(\alpha_1 \omega, SF_2)} \tag{3.23}$$

Here, S is the invariant measure of the strain rate, and it can be defined as $S = \sqrt{2S_{ij}S_{ij}}$. Furthermore, F_2 is the second blending function, and it can be computed using (3.24).

$$F_2 = \tanh\left[\left[max\left(\frac{2\sqrt{k}}{\beta^* \omega y}, \frac{500\nu}{y^2 \omega}\right)\right]^2\right] \tag{3.24}$$

Moreover, $\widetilde{P_k}$ can be determined as $\widetilde{P_k} = min(P_k, 10\beta^* \rho k\omega)$ where P_k can be computed using (3.25).

$$P_k = \rho \nu_{turb} \frac{\partial u_j}{\partial x_i}\left(\frac{\partial u_i}{\partial x_j} + \frac{\partial u_j}{\partial x_i}\right) \tag{3.25}$$

Furthermore, α_k, α_ω, α, and β coefficients can be computed using the blending function (F_1) which blends the coefficients between k-ω and k-ε turbulence model coefficients. As an example, (3.26) can be solved to determine α.

$$\alpha = F_1\alpha_1 + (1 - F_1)\alpha_2 \tag{3.26}$$

The other coefficients used in the k-ω *SST* turbulence model are as follows: $\beta^* = 0.09$, $\alpha_1 = 5/9, \beta_1 = 3/40$, $\sigma_{k1} = 0.85$, $\sigma_{\omega 1} = 0.5$, $\alpha_2 = 0.44$, $\beta_2 = 0.0828$, $\sigma_{k2} = 1$, $\sigma_{\omega 2} = 0.856$.

Stabilized k-ω SST Turbulence Model (Larsen and Fuhrman, 2018)

In the study of Larsen and Fuhrman (2018), it is stated that most of the commonly used turbulence models are unstable beneath the surface waves due to the overproduction of k and ν_{turb}. Therefore, standard forms of two-equation turbulence models are stabilized to prevent the non-physical values of k and ν_{turb} beneath the surface waves using a stress limiter by Larsen and Fuhrman (2018). Furthermore, the buoyancy production term proposed by Devolder et al. (2018) is also included in the k-ω *SST* turbulence model described by Menter et al. (2003). The equations of Stabilized k-ω *SST* model are given below. Although the equation of the specific dissipation rate (3.27) is analogous to (3.19), it is written again for consistency.

$$\frac{\partial \rho k}{\partial t} + \frac{\partial\left(\rho u_j k\right)}{\partial x_j} = \widetilde{P_k} - P_b - \rho\beta^* k\omega + \frac{\partial}{\partial x_j}\left[\left(\mu + \rho\sigma_k \nu_{turb}\right)\frac{\partial k}{\partial x_j}\right] \tag{3.27}$$

$$\frac{\partial \rho\omega}{\partial t} + \frac{\partial \left(\rho u_j \omega\right)}{\partial x_j}$$
$$= \alpha\rho S^2 - \rho\beta\omega^2 + \frac{\partial}{\partial x_j}\left[\left(\mu + \rho\sigma_\omega \nu_{turb}\right)\frac{\partial \omega}{\partial x_j}\right] \quad (3.28)$$
$$+ 2(1 - F_1)\rho\sigma_{\omega 2}\frac{1}{\omega}\frac{\partial k}{\partial x_j}\frac{\partial \omega}{\partial x_j}$$

Here, P_b is the buoyancy production term which can be computed using (3.29).

$$P_b = \nu_{turb}\alpha_b^*\frac{\partial \rho}{\partial x_i}g_i \quad (3.29)$$

Furthermore, the turbulent eddy viscosity (ν_{turb}) can be determined using (3.30).

$$\nu_{turb} = \frac{\alpha_1 k}{max\left(\alpha_1\omega, SF_2, \alpha_1\lambda_2\frac{\beta}{\beta^*\alpha}\frac{S^2}{P_\Omega}\omega\right)} \quad (3.30)$$

Here, P_Ω can be determined as $P_\Omega = 2\Omega_{ij}\Omega_{ij}$ where Ω_{ij} is the mean rotation rate tensor which can be computed using (3.31).

$$\Omega_{ij} = \frac{1}{2}\left(\frac{\partial u_i}{\partial x_j} - \frac{\partial u_j}{\partial x_i}\right) \quad (3.31)$$

In this turbulence model, α_b^* and λ_2 are chosen as 1.36 and 0.05, respectively. It should be noted that λ_2 is the stress limiter that prevents the excessive turbulent kinetic energy production near the potential flow region. Moreover, other coefficients are analogous to the k-ω SST turbulence model described by Menter et al. (2003).

3.1.1.6 Wall Functions

During the hydrodynamic studies, wall functions are applied for the turbulence parameters as boundary conditions to simulate the near-wall behavior of the flow. Besides the wall functions provided by OpenFOAM, two different boundary conditions described by Fuhrman et al. (2010) and Fuhrman et al. (2014) are used in

this part of the study. More detailed explanations about the wall functions are given below.

Wall Functions for Turbulent Kinetic Energy (k)

By default, OpenFOAM provides *kqRWallFunction* boundary condition, which applies a Neumann type boundary condition ($-\partial k/\partial y = 0$) for turbulent kinetic energy (k). Furthermore, Fuhrman et al. (2014) presented a Dirichlet boundary condition for k for smooth walls. Equations for the turbulent kinetic energy wall function presented by Fuhrman et al. (2014) are given below.

$$\frac{k}{U_f^2} = min\left\{A\Delta y^{+2}, \frac{1}{\sqrt{\beta^*}}\right\} \tag{3.32}$$

Here, U_f is the friction velocity that can be determined using the velocity profile described by Cebeci and Chang (1978), which is a generalized form of van Driest velocity profile (van Driest, 1956). Moreover, Δy^+ is expressed as $\Delta y^+ = \Delta y U_f/\nu$ where Δy is the cell thickness of the first cell. Furthermore, A is included in the equation to ensure an accurate scaling inside the viscous sublayer. (3.33) can be used to compute A.

$$A = \frac{1}{\delta^{+2}\sqrt{\beta^*}} \tag{3.33}$$

Here, δ^+ is the non-dimensional viscous sublayer thickness. It should also be noted that this parameter provides a smooth transition between the viscous sublayer and the logarithmic layer when $\Delta y^+ = \delta^+$.

Wall Functions for Specific Dissipation Rate (ω)

In OpenFOAM, *omegaWallFunction*, which applies a blending of viscous and log layer conditions described by Menter and Esch (2001) for ω, is provided. Equations for the *omegaWallFunction* boundary condition are given below.

$$\omega_{vis} = \frac{6\nu}{0.075y^2} \tag{3.34}$$

$$\omega_{log} = \frac{1}{0.3\kappa}\frac{U_f}{y} \tag{3.35}$$

$$\omega = \sqrt{{\omega_{vis}}^2 + {\omega_{log}}^2} \tag{3.36}$$

Here, ω_{vis} and ω_{log} are the specific dissipation rates in the viscous sublayer and logarithmic regions, respectively. Furthermore, U_f is the friction velocity, and κ is the Von Karman constant, which is chosen as $\kappa = 0.4$.

Furthermore, a different wall function explained by Wilcox (2006) and Fuhrman et al. (2010) is also studied. Equations for the specific dissipation rate are given below.

$$\omega = \frac{U_f}{\nu} S_r \tag{3.37}$$

$$S_r = \begin{cases} \left(\frac{K_s}{k_N^+}\right)^2, & k_N^+ \leq 5 \\ \frac{K_r}{k_N^+} + \left(\left(\frac{K_s}{k_N^+}\right)^2 - \frac{K_r}{k_N^+}\right) e^{5-k_N^+}, & k_N^+ > 5 \end{cases} \tag{3.38}$$

Here, K_s and K_r are the smooth and rough wall coefficients, and k_N^+ is expressed as $k_N^+ = k_N U_f/\nu$ where k_N is Nikuradse's sand roughness. During the hydrodynamic simulations, $K_s = 200$ and $K_r = 100$ are used for smooth wall boundaries, as suggested by Fuhrman et al. (2010).

Finally, another one explained by Fuhrman et al. (2014) is studied, and the model equation is given below.

$$\frac{\omega\nu}{U_f^2} = max\left\{\frac{B}{\Delta y^{+2}}, \frac{1}{\sqrt{\beta^*}\kappa\Delta y^+}\right\} \tag{3.39}$$

Furthermore, B is included in the equation to ensure an accurate scaling inside the viscous sublayer in addition to a smooth transition between layers. (3.40) can be used to compute B.

$$B = \frac{\delta^+}{\sqrt{\beta^*}\kappa} \tag{3.40}$$

Wall Functions for Turbulent Dissipation (ε)

In OpenFoam, the *epsilonWallFunction* boundary condition is provided for turbulent dissipation. It applies a fixed value for the cell centers by averaging the values at the cell faces. Model equations related to the *epsilonWallFunction* boundary condition are given below.

$$\varepsilon = \frac{1}{W}\sum_{f=i}^{W}\left(\frac{C_\mu^{0.75}k^{1.5}}{\kappa y_i}\right) \tag{3.41}$$

Here, W is the number of faces (f) that use the wall function in a cell. k is the turbulent kinetic energy, y is the distance from the wall, κ is taken as $\kappa = 0.4$ and C_μ is chosen as $C_\mu = 0.09$.

A detailed explanation about the wall functions is given by Liu (2016).

3.1.1.7 Wave Generation and Absorption

In most coastal engineering applications, wave generation and absorption are essential for a realistic simulation. Higuera et al. (2013) presented wave generation and active wave absorption boundary conditions inside the *IHFOAM* module. In the module, Stokes I, II, and V, cnoidal, streamfunction, solitary wave, and irregular wave theories are available for wave generation. Furthermore, a piston-type wavemaker can also be used to generate the waves using either the piston displacements, piston velocities, or the free surface time series. In this study, a piston-type wavemaker is used, and the piston movements are given to generate the waves analogous to those obtained in the laboratory experiments by Yaman (2022).

Furthermore, an active wave absorption boundary condition that minimizes the reflection of waves is used at both inlet and outlet boundaries. In the *IHFOAM*

module, there are several wave absorption boundary conditions. In this study, 2D wave absorption (Schaffer and Klopman, 2000) based on linear shallow-water theory is used. Detailed information about the active wave absorption theory is given by Higuera et al. (2013).

3.1.2 Numerical Model Settings

3.1.2.1 Review of the Experimental Setup (Yaman, 2022)

The physical experiments were carried on by Yildirim (2021) and Yaman (2022). In both studies, the same experimental setup was used, but the wave characteristics were different. In this study, experimental results obtained by Yaman (2022) are used. The physical experiments were performed in Middle East Technical University, Civil Engineering Department, Coastal and Ocean Engineering Laboratory, where the flume length is 19.6 m measured from the wave generator to the absorber, flume width is 6.0 m, and the flume depth is 1.0 m. The experimental setup and the wave gauges (WG) that are located to measure the free surface elevations are given in Figure 3.2.

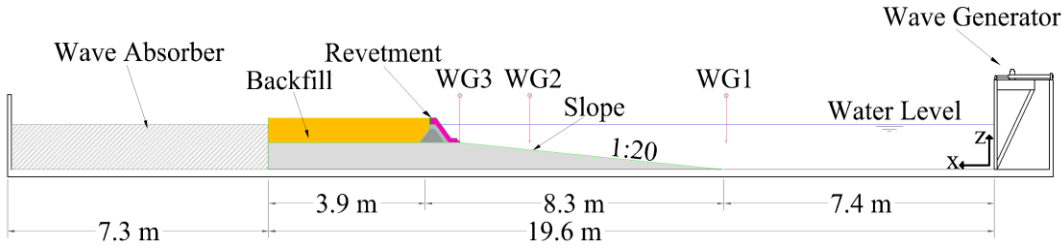

Figure 3.2: Experimental setup (Yildirim, 2021)

In the experimental setup, the bed slope is taken as 1:20, and the length of the backfill material is chosen as 3.9 m. In addition, the water depth is taken as 0.64 m. Waves are generated using a piston-type wave generator. At the end of the slope, a coastal revetment is placed, and its rear is filled with backfill material.

Moreover, a three-layer (armor, filter, and core) coastal revetment with a crown wall is used in the experimental studies by Yaman (2022). The dimensions and the details of the coastal revetment are given in Figure 3.3.

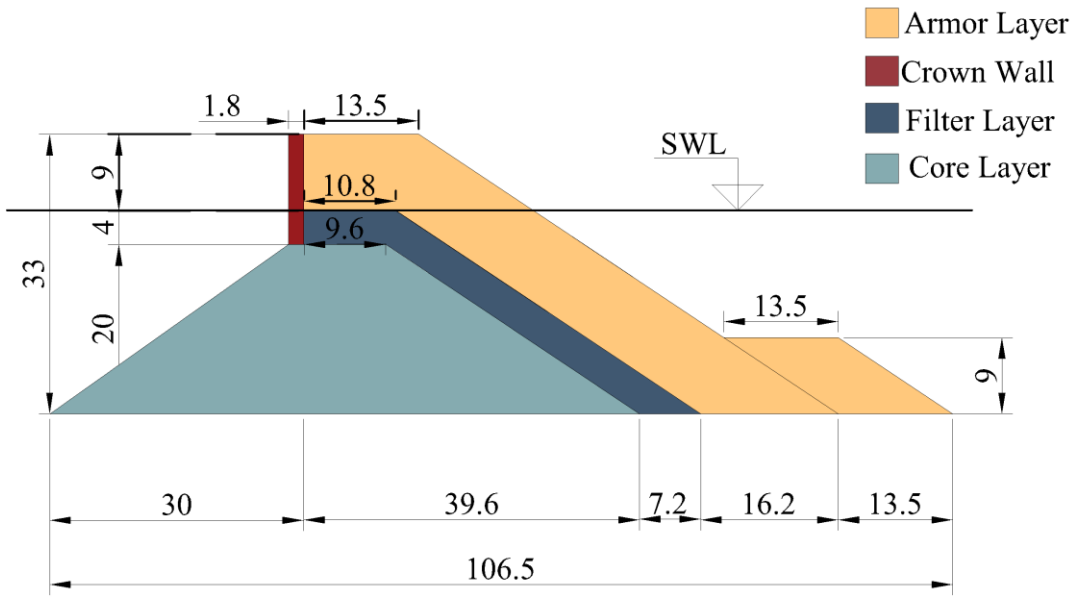

Figure 3.3: Coastal revetment model (dimensions are in cm)

In the experimental studies by Yildirim (2021) and Yaman (2022), the coastal revetment shown in Figure 3.3 is designed, and the stone sizes are determined using Hudson et al. (1979). The details about the physical properties of the coastal revetment stones and the backfill material are given in Table 3.1.

Table 3.1: Properties of the coastal revetment stones and the backfill material

Material	**Diameter of the Stones (D_{n50}) in cm**	**Porosity (ϕ)**
Armor	4.46	0.38
Filter	1.99	0.41
Core	1.30	0.41
Backfill Material	0.065	0.40

3.1.2.2 Computational Settings and Boundary Conditions

In this study, two-dimensional simulations are carried on since the experimental studies of Yildirim (2021) and Yaman (2022) can be considered as two-dimensional. Furthermore, the exact dimensions presented in Figure 3.2 and Figure 3.3 are used for the numerical simulations. To prepare the computational domain, *blockMesh* and *snappyHexMesh* utilities provided by OpenFOAM are used. First, a background mesh having a regular mesh size of 1 cm along the horizontal direction (*X*-axis) and 0.5 cm along the vertical direction (*Z*-axis) is prepared using *blockMesh* utility. In the transverse direction, one cell is used since two-dimensional simulations are carried on throughout this study. Then, the area beneath the bottom slope and the crown wall are removed from the computational domain using *snappyHexMesh* utility. Furthermore, cells sizes near the removed areas are halved such that 0.5 cm cell size along the horizontal direction and 0.25 cm cell size along the vertical direction is achieved. Finally, a refinement region shown in Figure 3.4 is defined near the coastal revetment area to compute the overtopping volumes more accurately. In this area, cell sizes are chosen as 0.25 cm and 0.125 cm along with the horizontal and vertical directions, respectively. The details of the computational domain and the cell sizes are given in Table 3.2.

Table 3.2 Properties of the Hydrodynamic Computational Domain

Location	Δx (cm)	Δz (cm)
General	1.0	0.5
Sloped Area	0.5	0.25
Crown Wall	0.5	0.25
Refinement Region	0.25	0.125

In the hydrodynamic part of this study, the following boundary conditions are applied for the simulations. The bottom boundary is chosen as a no-slip wall where the velocities are set to zero. At the inlet, piston-type wavemaker boundary

conditions described in Section 3.1.1.7 are used for the velocities and VOF function (γ). At the outlet, the active wave absorption boundary condition described in Section 3.1.1.7 is applied for the velocities. At the atmosphere, the *pressureInletOutletVelocity* boundary condition is used and set to zero for the velocities. This boundary applies a *zeroGradient* condition for the outflows and an obtained velocity value for the inflows. Moreover, this boundary condition allows the fluids to leave the computational domain. Furthermore, *buoyantPressure* boundary condition is used at the bottom, inlet, and outlet boundaries, and the pressure gradients are set to zero. For the atmosphere, *totalPressure* boundary condition is used such that the pressure is set to zero for the outflows, and it is determined by subtracting the dynamic pressure from the total pressure for the inflows. It is generally a common way to combine *pressureInletOutletVelocity* and *totalPressure* boundary conditions for the atmosphere where an inflow might occur, but the velocity of the inflow is not known. Finally, the back and front boundaries are set as *empty* so that the simulations can be carried on as two-dimensional. The details of the boundaries are given in Figure 3.4.

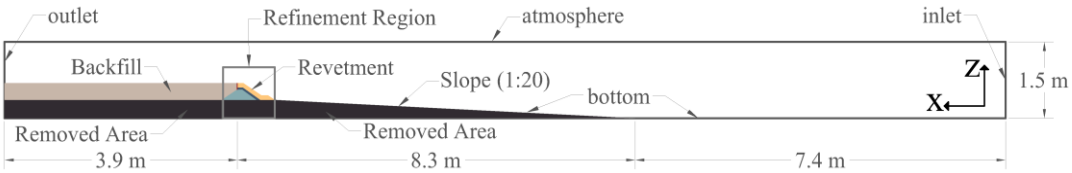

Figure 3.4: Computational domain and boundary conditions of the hydrodynamic studies

In the present study, simulation duration is selected as 20 seconds which is enough to observe the solitary wave overtopping. Furthermore, the results are written every 0.05 seconds. The total simulation time is approximately 24 hours with four Intel® Xeon® E7 v3 processor cores.

In both physical studies by Yaman (2022) and the numerical studies, the free surface elevation measurements are taken from the wave gauges shown in Figure 3.2, and the numerical results are compared with the observed ones. Furthermore, the overtopping measurements are taken from the top of the structure. To analyze the

measurements, velocity and γ values are used to compute the overtopping volumes. In these computations, the water phase is identified if γ is greater than 0.5. Then, the velocity values of the water phase are multiplied by the cell thicknesses to determine the discharges. Finally, the total overtopping volume is computed by summing the discharge values at each time step.

3.1.2.3 Mesh Independency

Grid dependency is an essential topic for numerical studies since the accuracy of the simulations depends on the mesh resolution. Roache (1998) suggested Grid Convergence Index (GCI) analysis to determine whether the mesh independence is satisfied or not. According to Roache (1998), GCI can be estimated using equation (3.42).

$$GCI = F_s|E| \tag{3.42}$$

Here, F_s is the factor of safety, which is taken as 3 as recommended by Roache (1998), and E is the Richardson error estimator, which can be calculated using equation (3.43).

$$E = \frac{\varepsilon}{1 - r^p} \tag{3.43}$$

Here r is the refinement factor, p is the formal order of accuracy of the algorithm, and ε is the difference between the numerical solutions obtained using coarse grid and fine grid. In this study, r is taken as 2 as recommended by Roache (1998), and p is determined as 2.

Throughout this study, the maximum values of the flow properties (velocity and turbulent kinetic energy) at the wave gauges are calculated for different grid sizes. Then, GCI values are determined, and the mesh sizes are refined until GCI is lower than %2. First, the mesh sizes are halved until GCI is close to the target value. Next, a refinement box is placed as it is presented in Figure 3.4, and this region is further refined rather than refining the whole domain so that the computational time can be

decreased. After the analysis, the mesh independence is satisfied for the mesh sizes given in Section 3.1.2.2.

3.1.2.4 Properties of the Simulations

In this study, the stone sizes and the porosity values which are needed to solve VARANS equations are analogous to the ones determined in the physical studies.

In the hydrodynamic part of the study, 3 different solitary wave heights (H) are studied for 6 different turbulence models. Furthermore, 2 different wall functions are studied for k-ω (Wilcox, 2006) simulations. Therefore, 21 different simulations are carried on in this part of the study. Furthermore, water depth (d) is set to 64.4 cm, which is analogous to the experimental setup for all studies. The details about the simulations are given in Table 3.3.

Table 3.3: Properties of the hydrodynamic simulations

Test No	**Turbulence Model**	**Wall Functions**	***H*** [1]
HD01	Laminar	-	8.6
HD02	k-ε (Launder and Sharma, 1974)	*kqRWallFunction* *epsilonWallFunction*	
HD03	Standard k-ω (Wilcox, 1988)	*kqRWallFunction* *omegaWallFunction*	
HD04	k-ω (Wilcox, 2006)	Fuhrman et al. (2014) for k Fuhrman et al. (2014) for ω	
HD05	k-ω (Wilcox, 2006)	*kqRWallFunction* Fuhrman et al. (2010) for ω	
HD06	k-ω *SST* (Menter et al., 2003)	*kqRWallFunction* *omegaWallFunction*	
HD07	Stabilized k-ω *SST* (Larsen and Fuhrman, 2018)	*kqRWallFunction* *omegaWallFunction*	
HD08	Laminar	-	9.6
HD09	k-ε (Launder and Sharma, 1974)	*kqRWallFunction* *epsilonWallFunction*	
HD10	Standard k-ω (Wilcox, 1988)	*kqRWallFunction* *omegaWallFunction*	
HD11	k-ω (Wilcox, 2006)	Fuhrman et al. (2014) for k Fuhrman et al. (2014) for ω	
HD12	k-ω (Wilcox, 2006)	*kqRWallFunction* Fuhrman et al. (2010) for ω	
HD13	k-ω *SST* (Menter et al., 2003)	*kqRWallFunction* *omegaWallFunction*	
HD14	Stabilized k-ω *SST* (Larsen and Fuhrman, 2018)	*kqRWallFunction* *omegaWallFunction*	
HD15	Laminar	-	10.2
HD16	k-ε (Launder and Sharma, 1974)	*kqRWallFunction* *epsilonWallFunction*	
HD17	Standard k-ω (Wilcox, 1988)	*kqRWallFunction* *omegaWallFunction*	
HD18	k-ω (Wilcox, 2006)	Fuhrman et al. (2014) for k Fuhrman et al. (2014) for ω	
HD19	k-ω (Wilcox, 2006)	*kqRWallFunction* Fuhrman et al. (2010) for ω	
HD20	k-ω *SST* (Menter et al., 2003)	*kqRWallFunction* *omegaWallFunction*	
HD21	Stabilized k-ω *SST* (Larsen and Fuhrman, 2018)	*kqRWallFunction* *omegaWallFunction*	
	[1] *Wave heights are measured at the toe of the structure in cm.*		

3.2 Morphological Model

3.2.1 Model Description and Governing Equations

As discussed in the previous chapter, OpenFOAM allows users to implement and use the existing packages developed by the other users. A fully coupled hydrodynamic and morphological model developed by Jacobsen (2011) is used in this part of the study. This model is capable of updating the bed morphology at each time step (optionally at user-defined time steps) considering the bed load and suspended load transports and sand-slide phenomenon. In this study, the existing solvers developed by Jacobsen (2011) are further developed to consider the free surface and the porous media effects. First, VOF methodology is implemented so that the free surface can be captured. Then, RANS equations are replaced with VARANS equations so that the porous media effects can also be considered.

In this study, simulations have been done in two steps (hydrodynamic and morphological studies). After the hydrodynamic studies, the required flow properties are taken from the top of the structure and inputted into the morphological model. Then, the hydrodynamic and morphological computations are done near the movable bed using the model. Simulating the problem in two steps has several physical and numerical purposes. The most important one is the high computational demand. As discussed by Baykal et al. (2017), simulation duration is about 14400 times higher than the physical duration for a single-phase steady current flow in a much smaller domain. It implies that this ratio will be much higher for the present study. On the other hand, simulating the problem in two steps reduced the computation time significantly because the morphological computations are done in a relatively small domain and only when there is an overtopping. Second, it is challenging to create a truncated domain (explained in Section 3.2.2.1) to solve suspended load equations if the bed morphology is relatively complex (bed with straight and sloped parts and the surface of rubble mound coastal revetment). On the other hand, when the problem is

simulated in two steps, a truncated domain is created only for the rear side of the coastal revetment, which has a straight bed.

In this part of the study, RANS equations given by (3.1) and (3.2) are solved by the model to determine the flow properties. For the morphological part, bed load and suspended load transport equations are solved, including the sand-slide effects.

3.2.1.1 Bed Load Transport

In the bed load transport computations, a separate mesh (Figure 3.5) is constructed (Jacobsen, 2011). In fact, bed load mesh is chosen as the bottom boundary since it occurs at the bottom. This transport module uses a finite volume methodology for general three-dimensional curved surfaces, and the methodology is also called as finite area method (FAM). The same mesh is also used for the updating routine, which is explained later in the section.

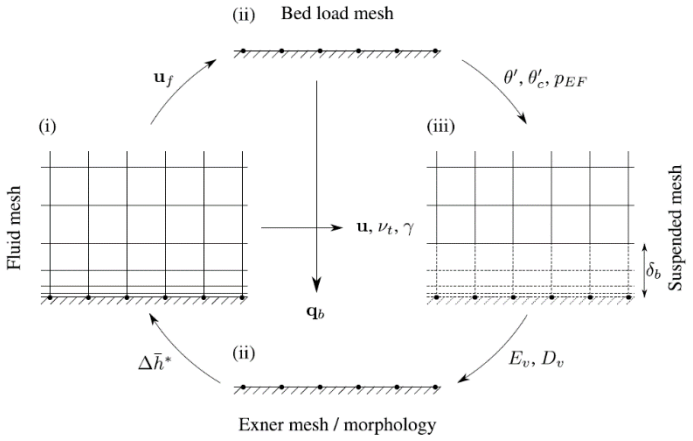

Figure 3.5: Model meshes to solve (i) RANS, (ii) bed load transport equation and sand continuity equation, (iii) suspended load transport equation (adopted from Jacobsen, 2011)

The model solves the bed load equations that were first developed by Engelund and Fredsoe (1976) and further extended by Roulund et al. (2005) to consider two-dimensional vectorial representation. To compute the bed load transport rate (q_b), (3.44) is solved by the model.

$$q_b = \frac{1}{6}\pi d^3 \frac{P_{EF}}{d^2} U_b \tag{3.44}$$

Here, d is the grain size, U_b is the mean transport velocity of the particle, and P_{EF} is the percentage of particles in motion in the surface layer of the bed, which can be computed using (3.45).

$$P_{EF} = \left(1 + \left(\frac{\frac{1}{6}\pi\mu_d}{\theta' - \theta_c'}\right)^4\right)^{-1/4} \tag{3.45}$$

In (3.45), θ' is the Shields parameter, and it can be computed using (3.46). Furthermore, θ_c' is the critical Shields parameter to initiate the motion, and it can be determined using (3.47). Finally, μ_d is the dynamic friction coefficient which is taken as 0.75 throughout the study.

$$\theta' = \frac{u_f^2}{(s-1)gd} \tag{3.46}$$

$$\theta_c' = \theta_{c0}'\left(\cos\beta\sqrt{1 - \frac{\sin^2\alpha\tan^2\beta}{\mu_s^2}} - \frac{\cos\alpha\sin\beta}{\mu_s}\right) \tag{3.47}$$

Here, s is the specific gravity of the grains, which can be computed as $s = \rho_s/\rho$ where ρ_s is the sediment density and ρ is the water density. Furthermore, u_f is the friction velocity, g is the gravitational acceleration, θ_{c0}' is the critical Shields parameter for a horizontal bed, and μ_s is the static friction coefficient. In this study, θ_{c0}' and μ_s are taken as 0.045 and 0.65, respectively. Finally, α is the angle between the directions of the flow and the bed slope (β), as shown in Figure 3.6.

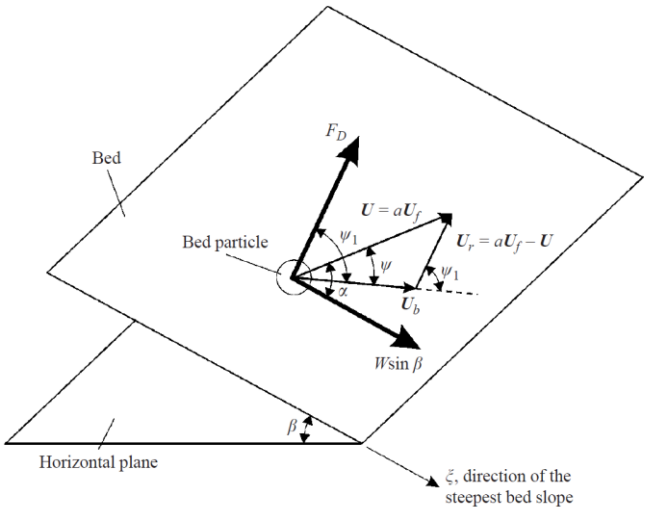

Figure 3.6: Forces acting on a particle on a sloped bed (adopted from Roulund et al., 2005)

The last unknown given in (3.44) is U_b. According to Roulund et al. (2005), it can be computed using a force balance equation consisting of the forces presented in Figure 3.6. The first one is the gravitational force (W_τ) which can be computed using (3.48).

$$W_\tau = \frac{1}{6}\pi\rho g(s-1)d^3 \sin\beta \tag{3.48}$$

The other force acting on the sediment particle is the combination of drag and lift forces (F_D), and it can be determined using (3.49).

$$F_D = \frac{1}{2}\rho c \frac{\pi}{4} d^2 U_r^2 \tag{3.49}$$

Here, U_r is the relative velocity of the flow, and it can be determined as $U_r = \alpha U_f - U_b$ where α is taken as 10. Furthermore, c is the force coefficient, and it can be computed using (3.50) as suggested by Fredsoe and Deigaard (1992).

$$c = \frac{4\mu_d}{3\alpha^2 \frac{1}{2}\theta'_{c0}} \tag{3.50}$$

Finally, the friction force (f_f) can be determined using (3.51).

$$f_f = W\cos\beta\,\mu_d \tag{3.51}$$

After determining all the forces acting on the sediment particle, a force balance equation can be written and solved using the vectorial forms of W_τ, F_D and f_f. Consequently, there will be 4 unknowns (including U_b) and 4 equations. Therefore, U_b can be computed by solving these equations. Then, q_b can be determined solving (3.44).

3.2.1.2 Sand Slide Phenomenon

According to Roulund et al. (2005), there might be a sliding phenomenon due to the shear failures in the flow direction if the bed slope becomes larger than the angle of repose. In this model, the procedure described by Niemann et al. (2011) is used to consider the sand slide phenomenon. According to Niemann et al. (2011), first, the grids where the slope exceeds the angle of repose are determined. Then, the grid points are rearranged until the prescribed value for the slope is achieved. Obviously, the volume of the sand will change after the rearrangements of the grid points. To satisfy the sand continuity, the removed volume of sand is determined, and the bed level corresponding to the grid points is raised such that the removed and the raised volumes of sand are equal to each other. In this study, the critical bed slope is chosen as 32^o such that the sand slide computations are started when the bed slope exceeds that limit, then the mesh is updated until the bed slope reaches a value lower than the critical one. According to Roulund et al. (2005), this phenomenon is instantaneous; therefore, the present calculations are stopped, and the sand slide computations are started when the sand slide occurs. Then, the new bed is determined, and the calculations are continued with the updated bottom. To summarize, a different time domain (apart from the hydrodynamic and morphological time domain) is used for the sand slide computations.

3.2.1.3 Suspended Sediment Transport

According to Fredsoe and Deigaard (1992), suspended sediment transport can be defined as the load that is not in contact with the bottom boundary continuously. Therefore, a different mesh called a truncated mesh (Figure 3.5) is needed to solve the suspended sediment transport equations. To create the truncated mesh, a reference level (b) is determined and the cells below this level are removed since the load in this region can be considered as bed load (Baykal et al., 2017). Inside the truncated domain, an advection-diffusion type suspended sediment transport equation (3.52) is solved.

$$\frac{\partial c}{\partial t} + \left(\gamma u_j - w_s \delta_{j3}\right)\frac{\partial c}{\partial x_j} = \frac{\partial}{\partial x_j}\left(\gamma \varepsilon \frac{\partial c}{\partial x_j}\right) \tag{3.52}$$

Here, c is the suspended sediment concentration, w_s is the settling velocity which can be determined using the methodology described by Fredsoe and Deigaard (1992), and δ is the Kronecker delta. Furthermore, γ is added to the equation to ensure that the suspended sediment particles remain in the water phase. Finally, ε can be computed as $\varepsilon = \beta \nu_{turb} + \nu$ where β is taken as 1 throughout this study.

As discussed above, suspended sediment transport equations are solved within a truncated domain. Because the cells below the reference level (b) are removed from the domain, a new bottom boundary condition is needed to solve (3.52). In this model, the bottom boundary condition for c developed by Engelund and Fredsoe (1976) is extended and used by Jacobsen (2011). The suspended sediment concentration at the reference level (c_b) can be determined using (3.53).

$$c_b = \frac{c_0}{\left(1 + \frac{1}{\lambda_b}\right)^3} \tag{3.53}$$

Here, c_0 is the maximum attainable volumetric concentration which is taken as 0.6 and λ_b is the linear concentration which can be determined by solving (3.54).

$$\lambda_b{}^2 = \frac{\kappa^2 \alpha_1^2}{0.013 s\theta'}\left(\theta' - \theta'_{c0} - \frac{\pi}{6}\mu_d P_{EF}\right) \tag{3.54}$$

3.2.1.4 Morphological Model and Mesh Updating

In the model, bed elevation and the mesh are updated using the bed load and suspended load transport rates by solving the sediment continuity equation (Exner Equation) given in (3.55).

$$\frac{\partial h_b}{\partial t} = -\frac{1}{1-\phi}[\nabla q_b + E_s + D_s] \tag{3.55}$$

Here, h_b is the bed elevation, q_b is the bed load transport, ϕ is the porosity of the sediment, E_s and D_s are erosion and deposition due to the suspended sediment transport, respectively.

According to Jacobsen (2011), bed elevation change due to the bed load is needed to be projected since the direction of the mesh updating routine and the direction of the solution of bed load transport are not analogous. Therefore, the model considers the effects of bed load and suspended load separately. In (3.56), the bed level change due to the bed load transport ($h_{b,b}$) is given.

$$\Delta h_{b,b} = -\frac{1}{1-\phi}\frac{\nabla q_b}{|n e_g|}\Delta t \tag{3.56}$$

Here, n is the bed normal unit vector and e_g is the unit vector parallel to the gravity.

On the other hand, the contribution of erosion and deposition ($h_{b,s}$) is given in (3.57).

$$\Delta h_{b,s} = -\frac{1}{1-\phi}\frac{D_v - E_v}{|e_g N|}\Delta t \tag{3.57}$$

Here, N is described as the area of the face. Furthermore, D_v and E_v can be determined using (3.58) and (3.59).

$$E_v = (\nu + \nu_{turb})N\nabla c \tag{3.58}$$

$$D_v = |(w_s + u)N|c_b \tag{3.59}$$

3.2.1.5 Wall Functions

For morphological studies, using a proper wall function is essential for an accurate simulation since turbulence is a significant contributor to sediment transport. Apart from the hydrodynamic part, wall functions are slightly modified since the bottom boundary is a rough bed rather than a smooth wall. First, rough wall coefficient (K_r) is chosen as $K_r = 180$ as it is suggested by Fuhrman et al. (2010). Furthermore, Nikuradse's roughness coefficients are appropriately changed. Finally, the velocity profiles for rough beds are used to determine the friction velocity, as further explained by Fuhrman et al. (2010).

3.2.2 Numerical Model Settings

3.2.2.1 Computational Domain and Boundary Conditions

As explained in the previous section, the bottom boundary is used as a new mesh for bed load transport computations and bed morphology updating routine (Figure 3.5). Furthermore, a truncated mesh is generated to determine the suspended load rates. During this part of the study, the computational domain and the boundary conditions given in Figure 3.7 are used. After the hydrodynamic studies, the outputs of the overtopping flow properties (velocity and turbulence parameters) are taken from the top of the structure during the overtopping, and these outputs are given as inputs to the sediment module. Therefore, a simple rectangular domain where the bottom boundary is chosen as the top of the backfill material is used throughout this study.

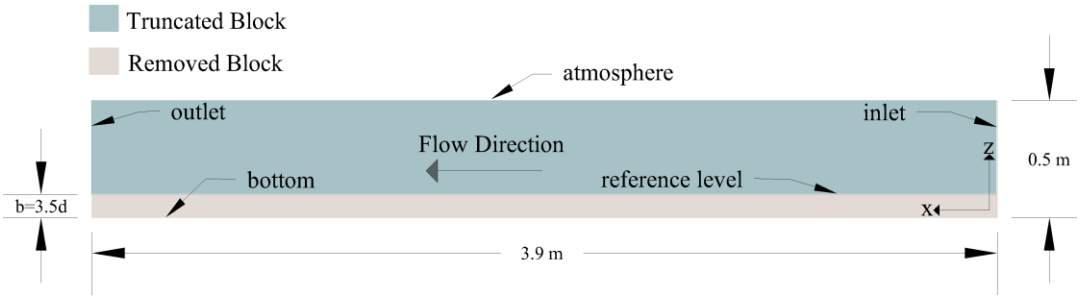

Figure 3.7: Computational domain and boundary conditions for sediment transport module (Not to scale.)

In this study, two-dimensional simulations are carried on since the scour phenomenon observed by Yaman (2022) can be considered as two-dimensional. To prepare the computational domain, *blockMesh* utility is used. The domain is divided into two parts: the truncated and removed blocks. The height of the removed block (b) is chosen as $b = 3.5d$, which is analogous to the values given by Baykal et al. (2017), where d is the diameter of the sediment particle. On the other hand, the height of the truncated block (t) is chosen as $t = 0.50\ m - 3.5d$. The cell size along the horizontal direction (X-axis) is chosen as 0.125 cm for both blocks. For the vertical direction (Z-axis) of the removed block, a uniform mesh is chosen such that the cell size is less than half of the diameter of the sediment particle ($d/2$). On the other hand, the *simpleGrading* methodology provided by OpenFOAM is used for the truncated block. Using *simpleGrading* methodology ensures a smooth transition between the blocks such that the first cell of the truncated block is equal to half of the diameter of the sediment particle ($d/2$) and the last cell of it is less than 0.25 cm. During the simulations, mesh sizes along the vertical axis are chosen carefully to ensure that the wall functions can be appropriately applied. Detailed information about the cell sizes is given in Table 3.4.

Table 3.4 Properties of the Morphological Computational Domain

Location	Domain Height (mm)	First Cell Size (mm)	Last Cell Size (mm)	Number of Cells
Removed Block	2.3	0.28	0.28	8
Truncated Block	497.7	0.28	2.19	47

In the morphological part of this study, the following boundary conditions are applied for the numerical simulations. For the atmosphere, a zero-flux condition is applied. Moreover, the reference concentration (c_b) for the suspended sediment concentration is used at the bottom boundary. An *empty* boundary condition is used for the back and front faces to satisfy a two-dimensional simulation. Finally, the *zeroGradient* condition is applied for the other boundaries.

During this part of the study, simulation duration is selected as 2 seconds which is enough to observe the scouring due to an individual solitary wave. Furthermore, the results are written at every 0.05 seconds. It should be noted that both hydrodynamic and morphological time steps are analogous to each other such that the bed morphology is updated at each time step. The total simulation time is approximately 4 hours with four Intel® Xeon® E7 v3 processor cores .

In this part of the study, the bed morphology is determined, and the results are compared with the experimental results by Yaman (2022). The comparisons are carried out for 4 different scour hole properties: the profile of the bed, the depth of the scour hole, the length of the scour hole, and the distance of the deepest point to the crown wall.

3.2.2.2 Properties of the Simulations

In this part of the study, inputs that are obtained from the hydrodynamic simulations are studied. An overall workflow is presented schematically in Figure 3.8.

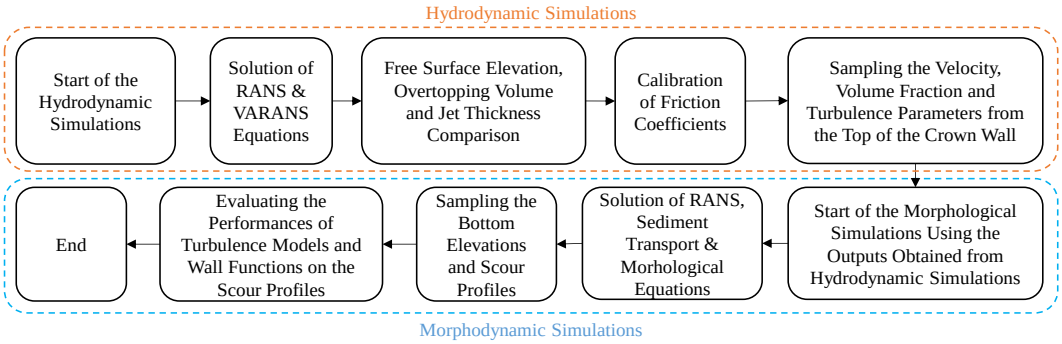

Figure 3.8. Overall workflow

To ensure consistency, the turbulence models and the wall functions are chosen as analogous to the ones that are used in the hydrodynamic part, except for the rough bed modifications. Turbulence models and the wall functions of the morphological simulations are given in Table 3.5. It should be noted that in the morphological studies, only H=8.6 cm simulations are carried on due to the high computational demand. The morphological simulations for the different wave heights presented in the hydrodynamic studies are left as a future study.

Table 3.5 Properties of the morphological simulations

Test No	**Turbulence Model**	**Wall Functions**	***H*** [1]
MD01	Laminar	-	8.6
MD02	k-ε (Launder and Sharma, 1974)	*kqRWallFunction* *epsilonWallFunction*	
MD03	Standard k-ω (Wilcox, 1988)	*kqRWallFunction* *omegaWallFunction*	
MD04	k-ω (Wilcox, 2006)	Fuhrman et al. (2014) for k Fuhrman et al. (2014) for ω	
MD05	k-ω (Wilcox, 2006)	*kqRWallFunction* Fuhrman et al. (2010) for ω	
MD06	k-ω *SST* (Menter et al., 2003)	*kqRWallFunction* *omegaWallFunction*	
MD07	Stabilized k-ω *SST* (Larsen and Fuhrman, 2018)	*kqRWallFunction* *omegaWallFunction*	
	[1] *Wave heights are measured at the toe of the structure in cm.*		

CHAPTER 4

RESULTS

In this section, simulation results are given in two parts. In the first part, hydrodynamic results are discussed in terms of the free surface elevations, overtopping volumes, and jet thicknesses. The second part gives morphological results with the bed profiles and the scour hole properties.

4.1 Hydrodynamic Results

In this part of the study, the numerical results of the hydrodynamic simulations are compared with the experimental results obtained by Yaman (2022) for calibration and validation purposes. First, the free surface elevations taken from the wave gauges are compared, and the porous media coefficients are calibrated. Then, the overtopping volumes and the jet thicknesses are compared with the experimental results. Furthermore, the effects of the turbulence models and wall functions on the hydrodynamic results are discussed.

4.1.1 Calibration of Porous Media Coefficients and Comparison of Free Surface Elevations

As it is discussed in Yildirim (2021), the free surface elevations and the overtopping volumes are important parameters that affect the scour profiles. Therefore, porous media coefficients are calibrated to get realistic hydrodynamic and morphological simulations. In this study, the optimum values are determined by comparing the numerical results with the experimental ones. First, the values suggested by Jensen et al. (2014) are studied during the calibration procedure for H=8.6 cm. Then, the parameters are changed individually until the variations in the free surface elevations

and the overtopping volumes are less than 2%. Finally, different wave heights are studied by using the same calibrated coefficients to validate the model. The calibrated porous media coefficients for each material are given in Table 4.1.

Table 4.1: Calibrated porous media coefficients

Material	$\boldsymbol{\alpha}$	$\boldsymbol{\beta}$	$\boldsymbol{C}$
Armor	10	0.6	0.34
Filter	20	0.7	0.34
Core	10	0.5	0.34
Backfill Material	10	0.5	0.34

After determining the optimum porous media coefficients, simulations are carried on again to obtain the free surface elevations, turbulent kinetic energies, eddy viscosities, overtopping volumes, and jet thicknesses.

In Figure 4.1, the comparison of free-surface elevations (η) for HD01-HD07 simulations where H=8.6 cm taken from WG3 (see Figure 3.2) is presented. In the figures, first, a comparison of all turbulence models is shown (a), then the results are separated (b, c, d) for a better presentation.

It should be noted that abbreviations (*WF-I* and *WF-II*) are used to represent the wall functions explained by Fuhrman et al. (2014) and Fuhrman et al. (2010), respectively, for the rest of the study.

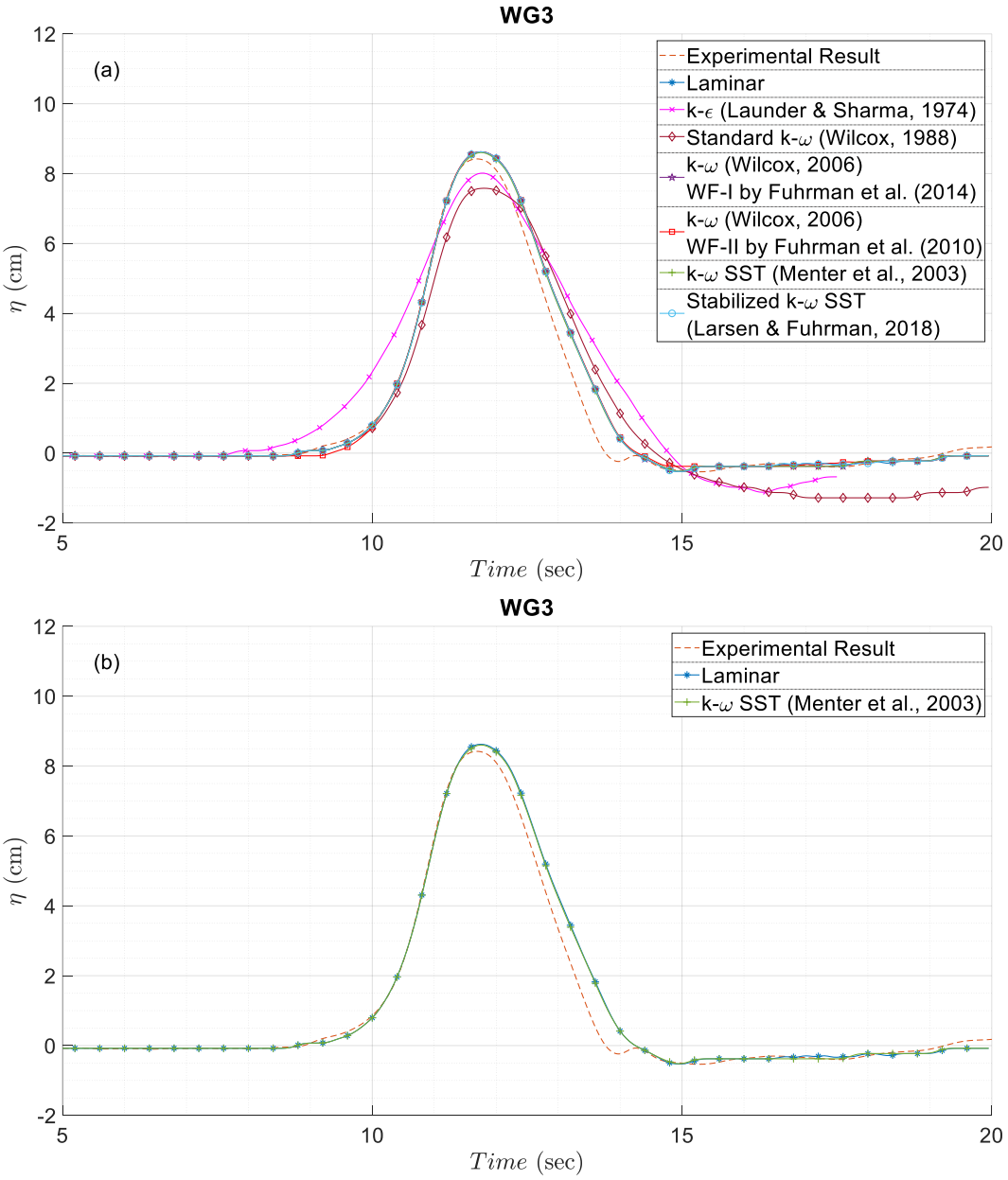

Figure 4.1: Comparison of free surface elevations for H=8.6 cm at WG3, (a) all turbulence models, (b) laminar and *k-ω SST*, (c) *k-ε*, *k-ω WF-I*, and *k-ω WF-II*, (d) standard *k-ω* and stabilized *k-ω SST*

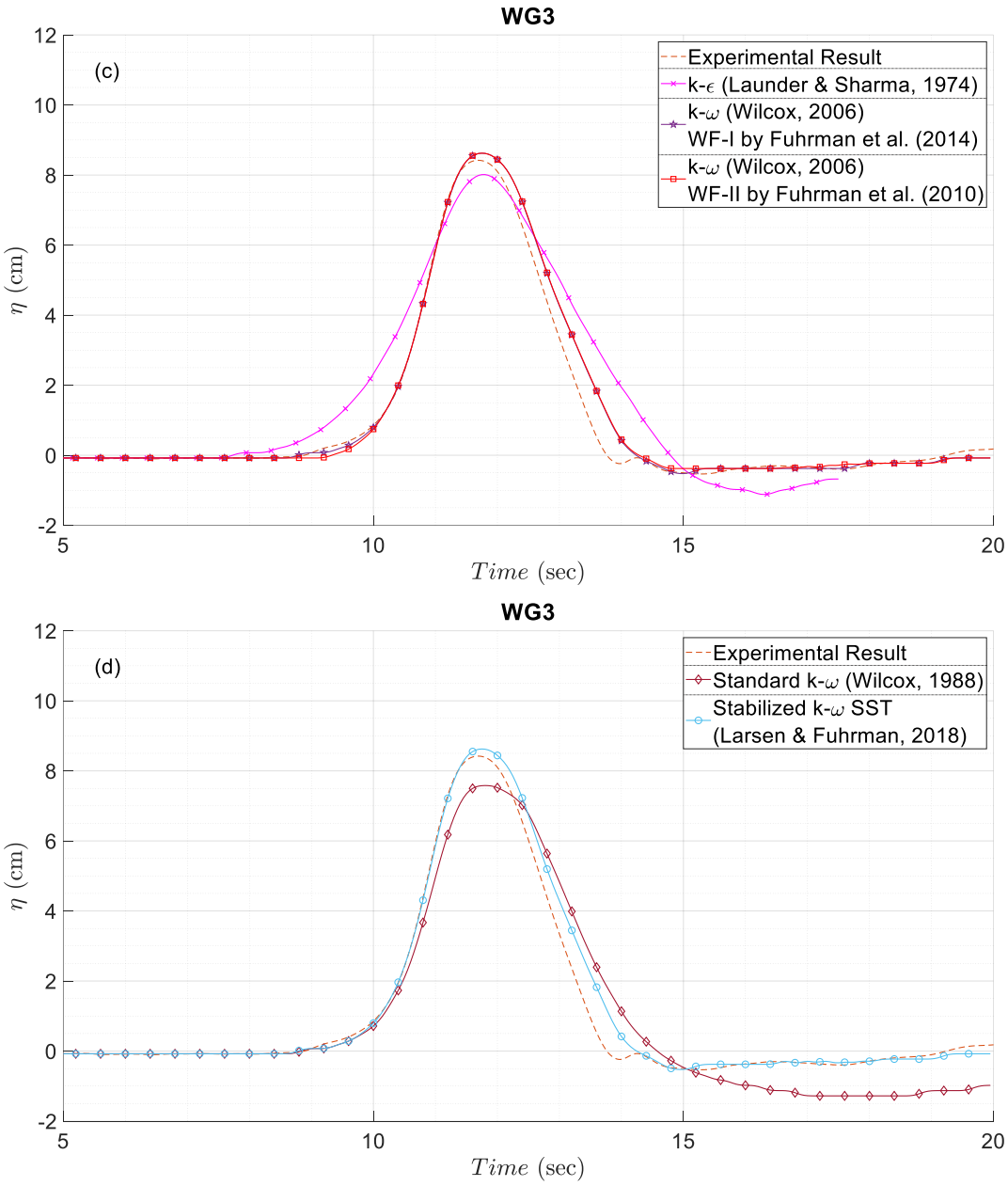

Figure 4.1 (Continued)

In Figure 4.1 (a), except for the k-ε and standard k-ω models, all turbulence models show good agreements with the physical model results regarding the water surface elevations. According to Bardina et al. (1997), the k-ε turbulence model is useful when there is a shear-free flow which is not analogous to this study. Furthermore, Figure 4.2 and Figure 4.3 show that k and ν_{turb} values are much higher for k-ε and standard k-ω models than the others. Qu et al. (2021) explain that higher turbulent kinetic energy and eddy viscosity values consume more energy from the total energy. Therefore, about %20 smaller water surface elevation peaks are obtained for k-ε and standard k-ω models. On the other hand, peaks obtained from the laminar simulations are the highest ones since the turbulence does not consume the total energy. It is also shown in Figure 4.1 (c) that using different wall functions does not affect the free surface elevations since the main interest is not directly related to the near-wall behavior.

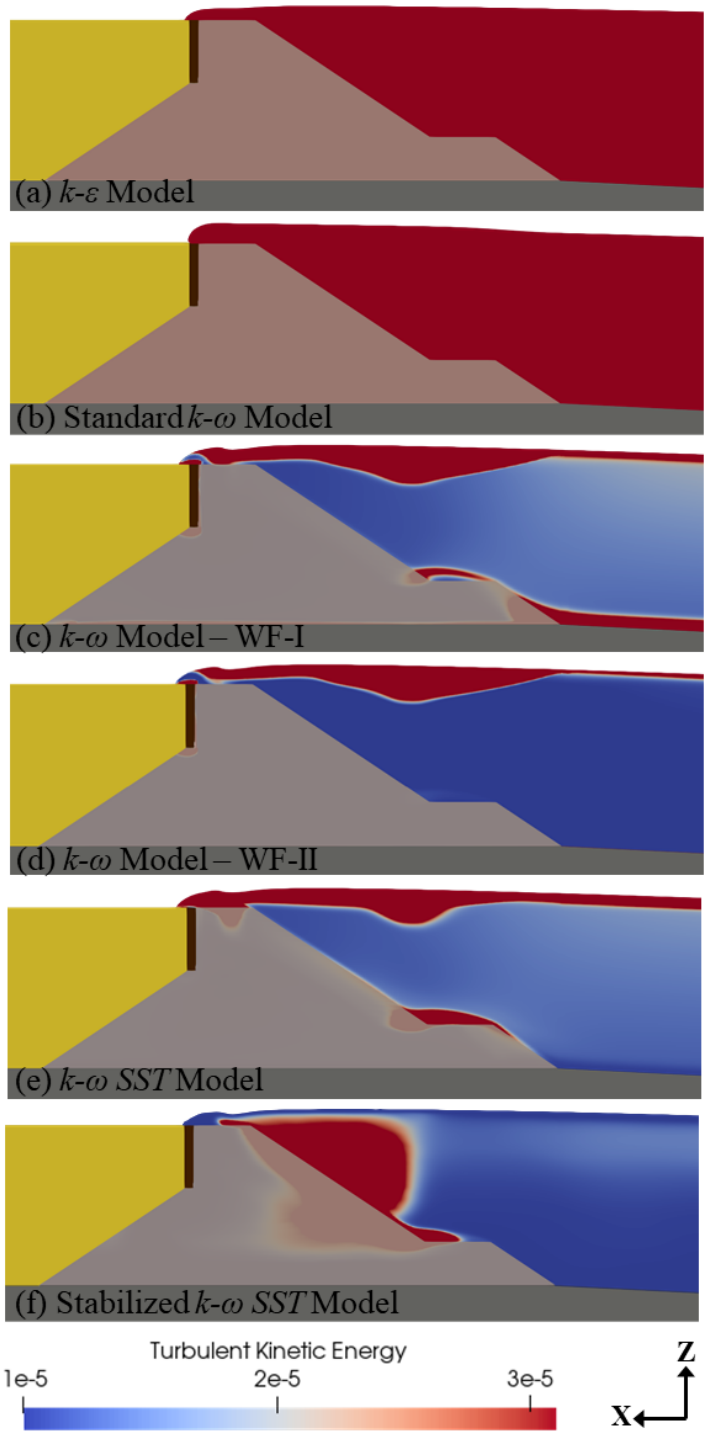

Figure 4.2: Turbulent kinetic energy (m^2/s^2) snapshots for H=8.6 cm, (a) *k-ε*, (b) standard *k-ω*, (c) *k-ω WF-I*, (d) *k-ω WF-II*, (e) *k-ω SST*, (f) stabilized *k-ω SST*

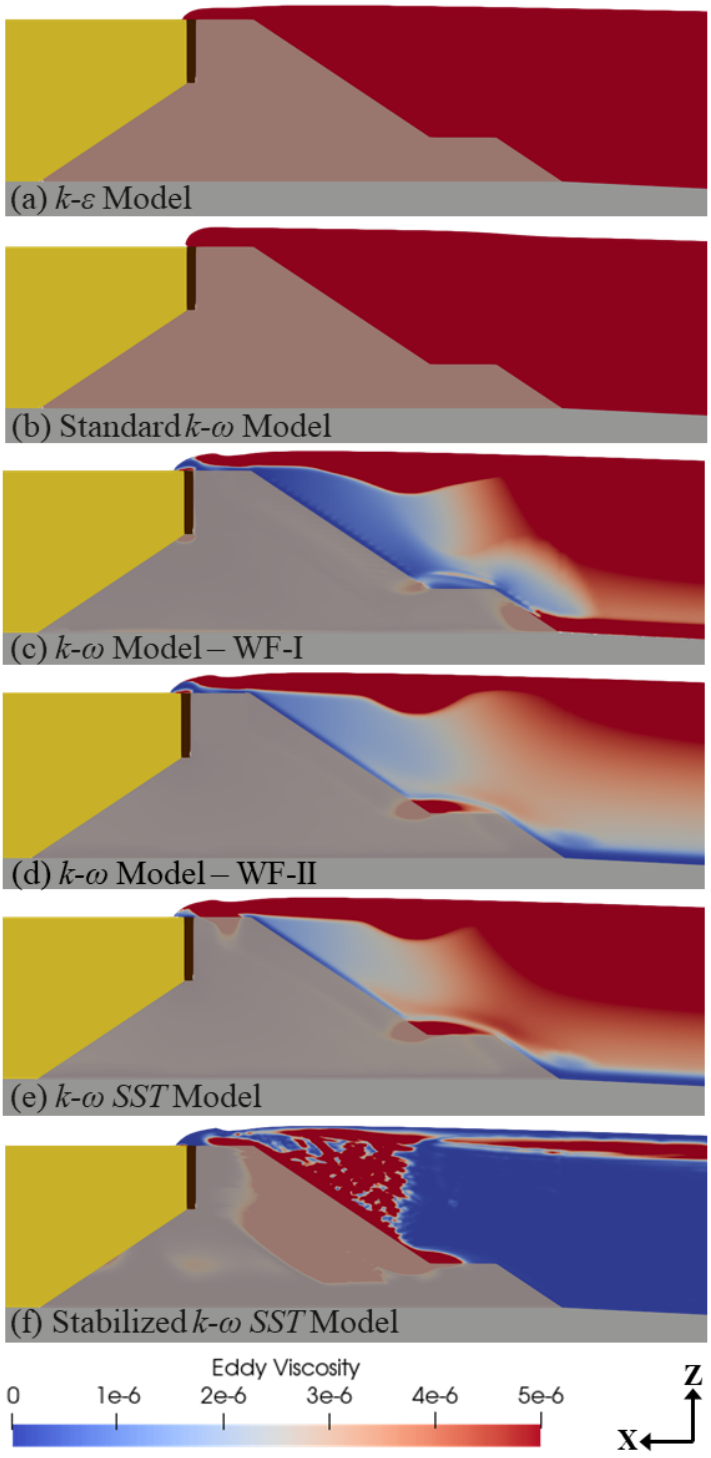

Figure 4.3: Eddy viscosity (m^2/s) snapshots for H=8.6 cm, (a) k-ε, (b) standard k-ω, (c) k-ω *WF-I*, (d) k-ω *WF-II*, (e) k-ω *SST*, (f) stabilized k-ω *SST*

In Figure 4.2 (f), it can be seen that the stabilized k-ω SST turbulence model reduces the turbulent kinetic energy significantly near the free surface region since the model includes a buoyancy production term. According to Qu et al. (2021), this term prevents the high turbulent kinetic energy values beneath the free surface. On the other hand, Figure 4.2 (c), Figure 4.2 (d), and Figure 4.2 (e) show that using k-ω and k-ω SST turbulence models yield very similar turbulent kinetic energy results during the hydrodynamic simulations. It is also noted by Baykal et al. (2017) that the authors experienced very similar trends between k-ω and k-ω SST turbulence models. In Figure 4.3 (c), it is observed that the stabilized k-ω SST closure reduces the eddy viscosity over the depth while k-ω and k-ω SST closures produced more eddy viscosity near the free surface. It can also be noted that the cross-diffusion and the stress limiter terms in the k-ω model reduce both the turbulent kinetic energy and the eddy viscosity significantly compared to the standard k-ω model. Furthermore, Figure 4.2 (c-d) illustrate that using different wall functions does not affect the turbulent kinetic energy significantly near the free surface region. Yet, there is a difference in the near-wall region.

In addition to HD01-HD07 results, HD08-HD14 and HD15-HD21 results are also presented to investigate whether there is an influence of the wave heights on the results. In Figure 4.4 and Figure 4.5, the comparisons of free-surface elevations for H=9.6 cm and H=10.2 cm taken from WG3 (see Figure 3.2) are presented, respectively.

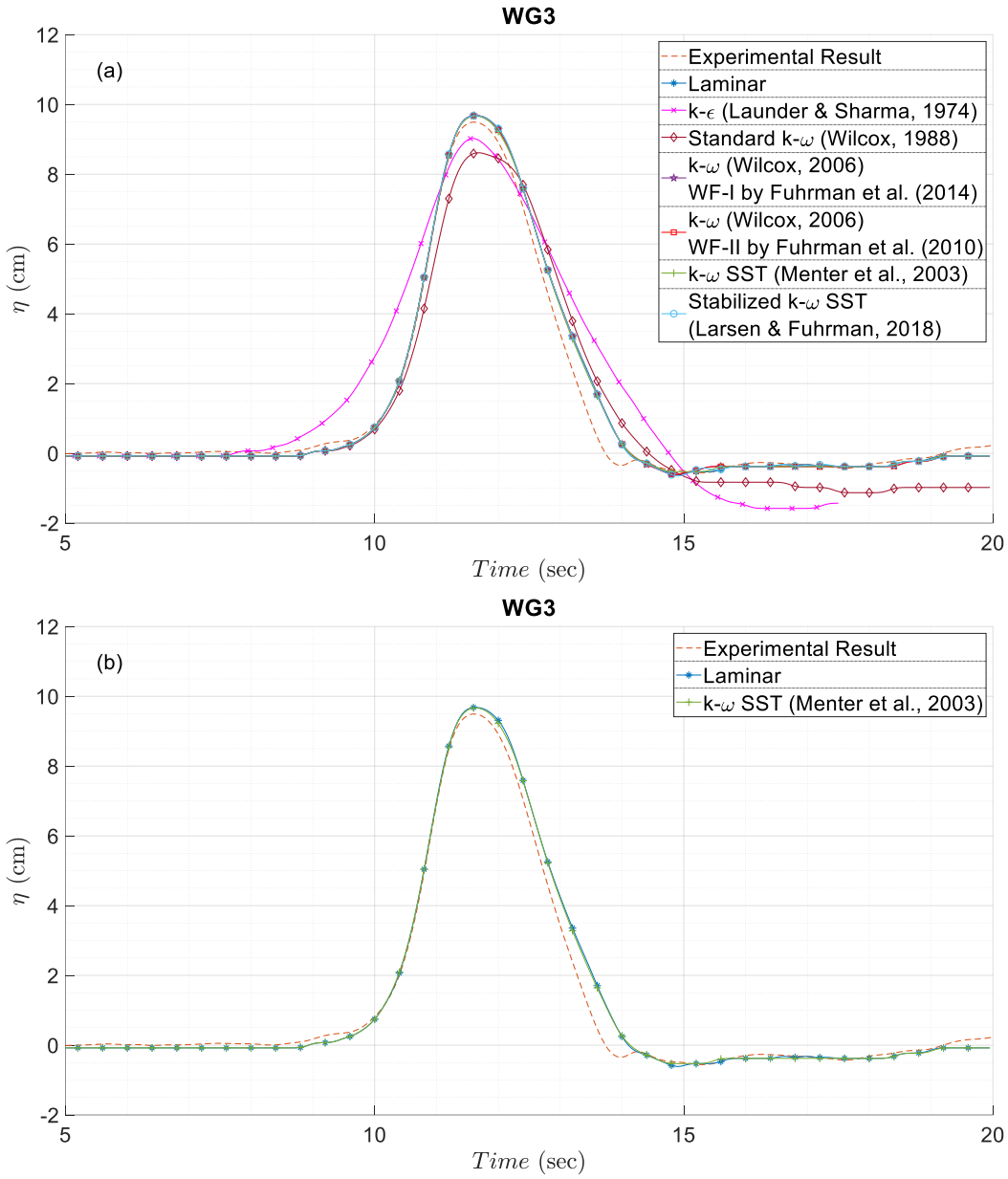

Figure 4.4: Comparison of free surface elevations for H=9.6 cm at WG3, (a) all turbulence models, (b) laminar and *k-ω SST*, (c) *k-ε*, *k-ω WF-I*, and *k-ω WF-II*, (d) standard *k-ω* and stabilized *k-ω SST*

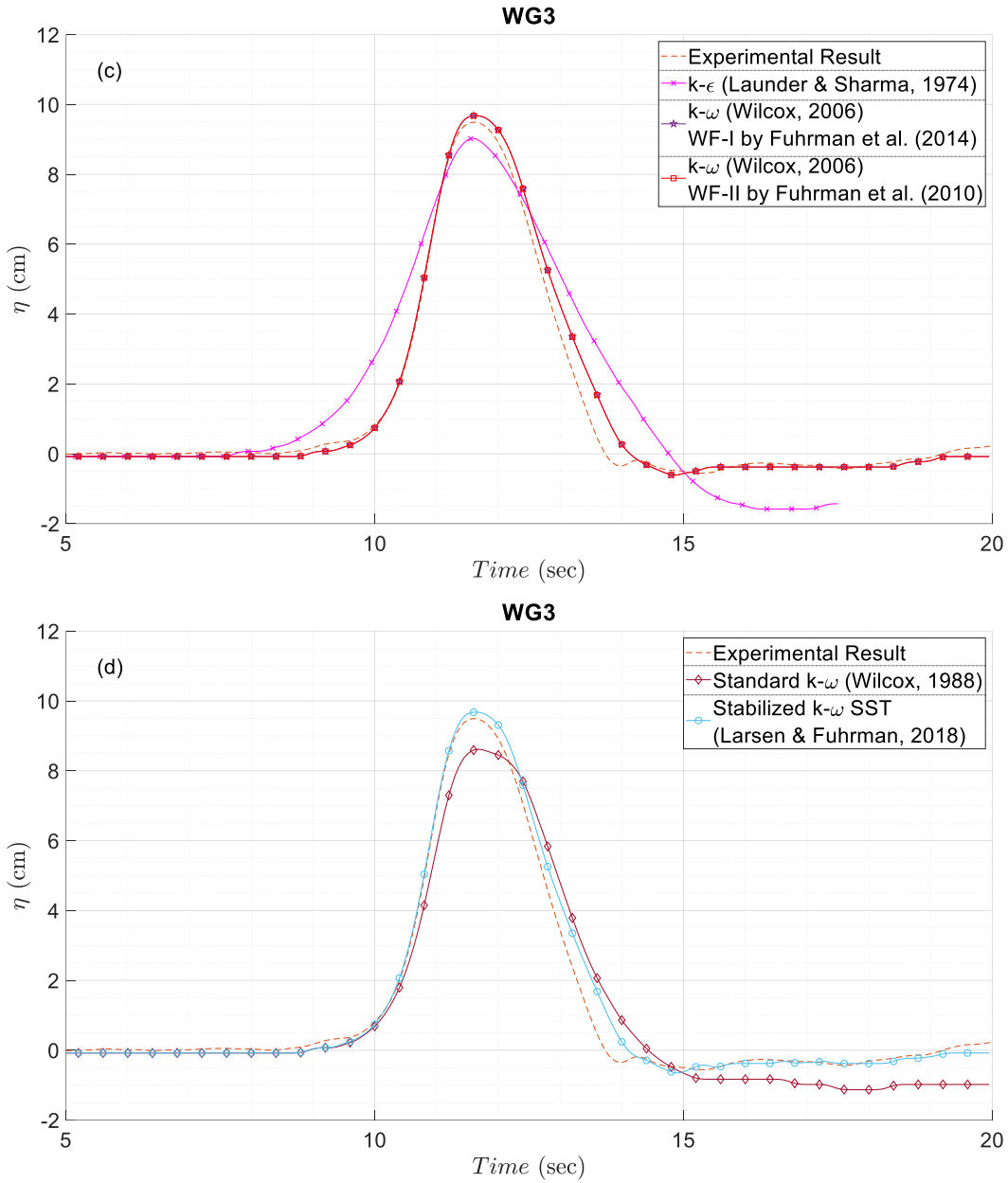

Figure 4.4 (Continued)

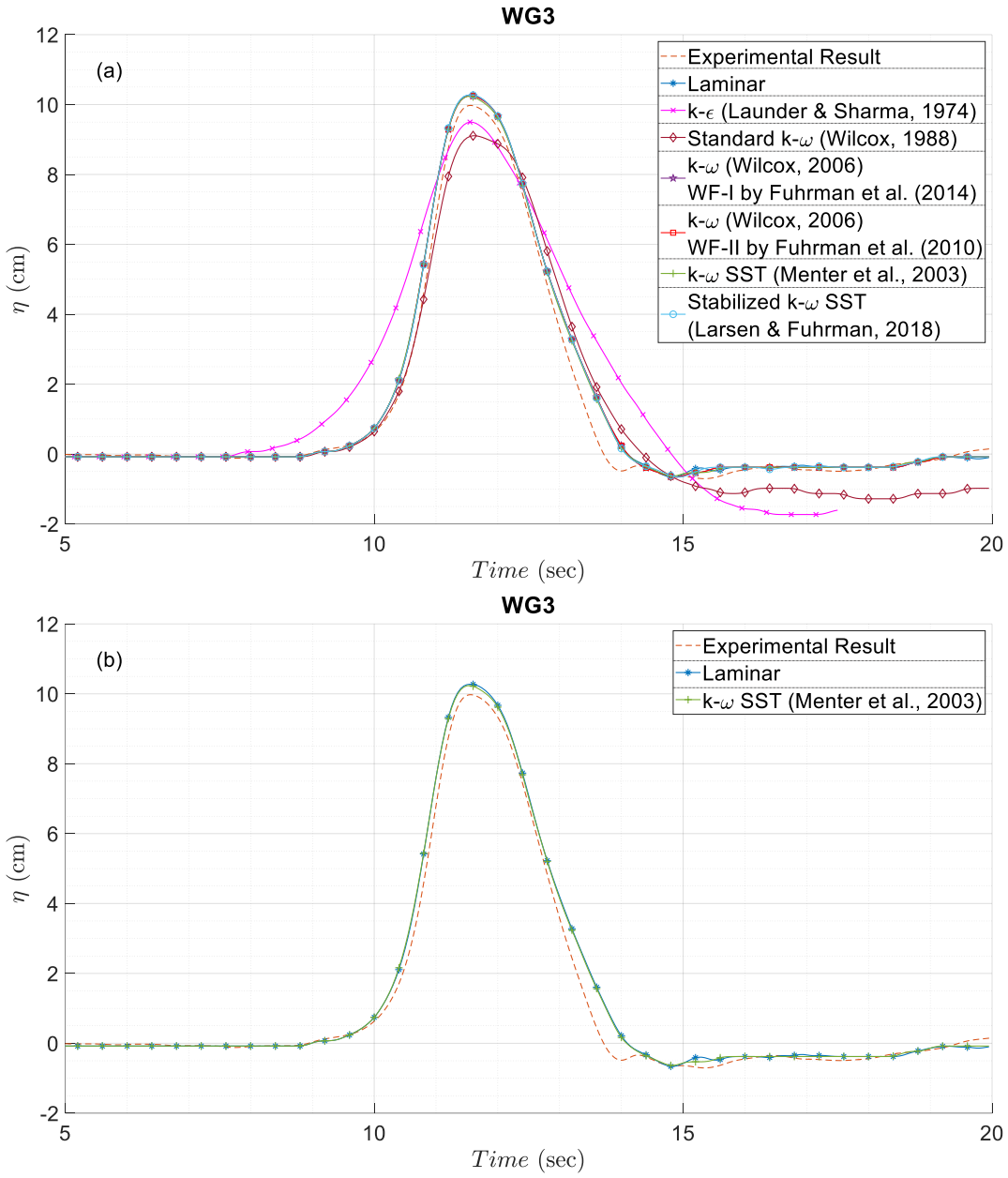

Figure 4.5: Comparison of free surface elevations for H=10.2 cm at WG3, (a) all turbulence models, (b) laminar and *k-ω SST*, (c) *k-ε*, *k-ω WF-I*, and *k-ω WF-II*, (d) standard *k-ω* and stabilized *k-ω SST*

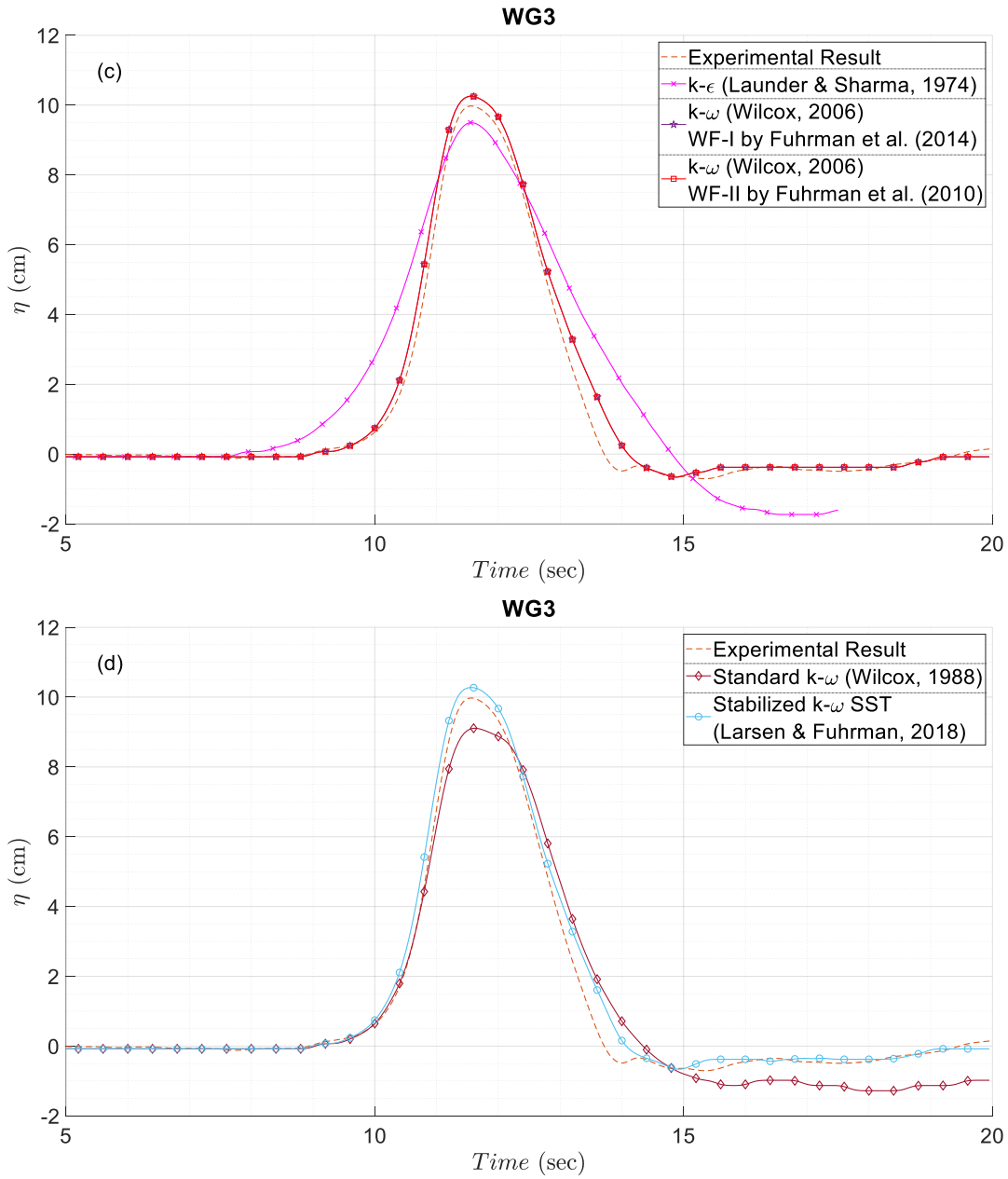

Figure 4.5 (Continued)

In Figure 4.4 and Figure 4.5, it can be seen that the trend for different solitary wave heights is very similar to each other. Although the wave heights are increased about %10 on average, there was no change in the trends of the hydrodynamic results.

Finally, a root mean square error methodology is used to measure the difference between the numerical and experimental results. Equations to determine the normalized root mean square error (NRMSE) values are given in below.

$$NRMSE = \frac{\sqrt{\frac{\sum_{i=1}^{T}\left(\eta_i^{num} - \eta_i^{exp}\right)^2}{T}}}{\eta_{max}^{num} - \eta_{min}^{num}} \tag{4.1}$$

Here, η_i^{num} and η_i^{exp} are the numerical and experimental free surface elevations at i^{th} points, respectively. Furthermore, T is defined as the total number of points. In Table 4.2, NRMSE values for the free surface elevations taken at WG3 are given.

Table 4.2 Normalized root mean square error (NRMSE) for WG3

	NRMSE		
	***H*=10.2[1]**	***H*=9.6[1]**	***H*=8.6[1]**
Laminar	0.0230	0.0237	0.0256
k-ε	0.0757	0.0721	0.0624
Standard *k-ω*	0.0338	0.0414	0.0463
k-ω WF-I	0.0232	0.0234	0.0255
k-ω WF-II	0.0232	0.0234	0.0264
k-ω SST	0.0222	0.0224	0.0246
Stabilized *k-ω SST*	0.0229	0.0234	0.0256

[1] *Wave heights are measured at the toe of the structure in cm.*

In Table 4.2, it can be seen that all turbulence closures except k-ε and standard k-ω show similar NRMSE values. Furthermore, it is observed that NRMSE values of the k-ε model is twice as the ones for the standard k-ω model.

4.1.2 Overtopping Volumes and Jet Thicknesses

After the simulations are completed, the results are analyzed using a MATLAB code to compute the overtopping volumes (Q) and the jet thicknesses. Numerical model results are compared with the experimental ones determined by Yaman (2022). In the studies of Yaman (2022), the same experimental simulation is repeated three times to obtain consistent results. According to Yildirim (2021), the governing parameter of the scour process is determined as the overtopping volume. Therefore, it is essential to capture the overtopping volume and jet thickness values accurately. The experimental results by Yaman (2022) and the numerical results for different wave heights are given in Table 4.3.

Table 4.3: Overtopping volumes and jet thicknesses

	Q (lt/m)			**Jet Thickness (cm)**		
	***H*=10.2[1]**	***H*=9.6[1]**	***H*=8.6[1]**	***H*=10.2[1]**	***H*=9.6[1]**	***H*=8.6[1]**
Experimental Result #1	35.3	29.2	20.1	5.6	5.2	4.3
Experimental Result #2	34.9	28.9	19.9	5.4	5.0	4.2
Experimental Result #3	35.1	28.6	19.8	5.5	4.7	4.0
Average of Experimental Results	35.1	28.9	19.9	5.5	4.9	4.1
Laminar	35.8	29.6	19.3	5.0	4.6	3.7
k-ε	15.5	11.8	7.1	3.3	3.0	2.2
Standard *k-ω*	33.5	22.7	9.6	7.1	6.3	4.3
k-ω WF-I	35.4	29.2	18.7	5.2	4.7	3.8
k-ω WF-II	35.4	29.2	18.7	5.2	4.7	3.8
k-ω SST	35.0	28.9	18.0	5.0	4.6	3.6
Stabilized *k-ω SST*	35.8	29.5	18.8	5.2	4.6	3.7

[1] *Wave heights are measured at the toe of the structure in cm.*

Furthermore, a mean absolute percentage error (MAPE) methodology is used to measure the accuracy of the turbulence models to predict the overtopping volumes and the jet thicknesses. Equations to determine the MAPE values are given in below.

$$MAPE = \left| \frac{X_{exp} - X_{num}}{X_{exp}} \right| \times 100 \quad (4.2)$$

Here, X_{exp} is the actual value which is determined by averaging the experimental results. Furthermore, X_{num} is the numerical value obtained from the simulations. MAPE values for overtopping volumes and the jet thicknesses are given in Table 4.4.

Table 4.4 MAPE of the overtopping volumes and the jet thicknesses

	MAPE of Q (%)			**MAPE of the Jet Thickness (%)**		
	***H*=10.2[1]**	***H*=9.6[1]**	***H*=8.6[1]**	***H*=10.2[1]**	***H*=9.6[1]**	***H*=8.6[1]**
Laminar	2.0	2.1	3.0	9.1	6.1	9.8
k-ε	55.8	59.3	64.3	40.0	38.8	46.3
Standard *k-ω*	4.6	21.7	51.8	29.1	28.6	4.9
k-ω WF-I	0.9	0.7	6.0	5.5	4.1	7.3
k-ω WF-II	0.9	0.7	6.0	5.5	4.1	7.3
k-ω SST	0.3	0.3	9.6	9.1	6.1	12.2
Stabilized *k-ω SST*	2.0	1.7	5.5	5.5	6.1	9.8

[1] *Wave heights are measured at the toe of the structure in cm.*

In Table 4.3 and Table 4.4, it is observed that the results of stabilized k-ω SST, k-ω SST, k-ω, and laminar simulations show good agreements with the experimental results in terms of both the overtopping volumes and the jet thicknesses. Furthermore, both wall functions showed similar results. Moreover, these turbulence models also matched well with the experimental results in terms of the free surface elevations, as it is discussed previously (Figure 4.1). In contrast, the k-ε turbulence model shows poor performance for both results. It predicts about %50 lower values for both overtopping volumes and the jet thicknesses. On the other hand, standard k-

ω simulations show very similar overtopping values to the experimental results. However, the jet thicknesses are over-predicted for this turbulence model. It is also noted that the overtopping durations determined for the standard k-ω turbulence model are about %30 higher compared to the other turbulence models. To understand this phenomenon, vertical variations of horizontal and vertical velocities are calculated from the top of the structure when the jet thicknesses are maximum (Figure 4.6 and Figure 4.7).

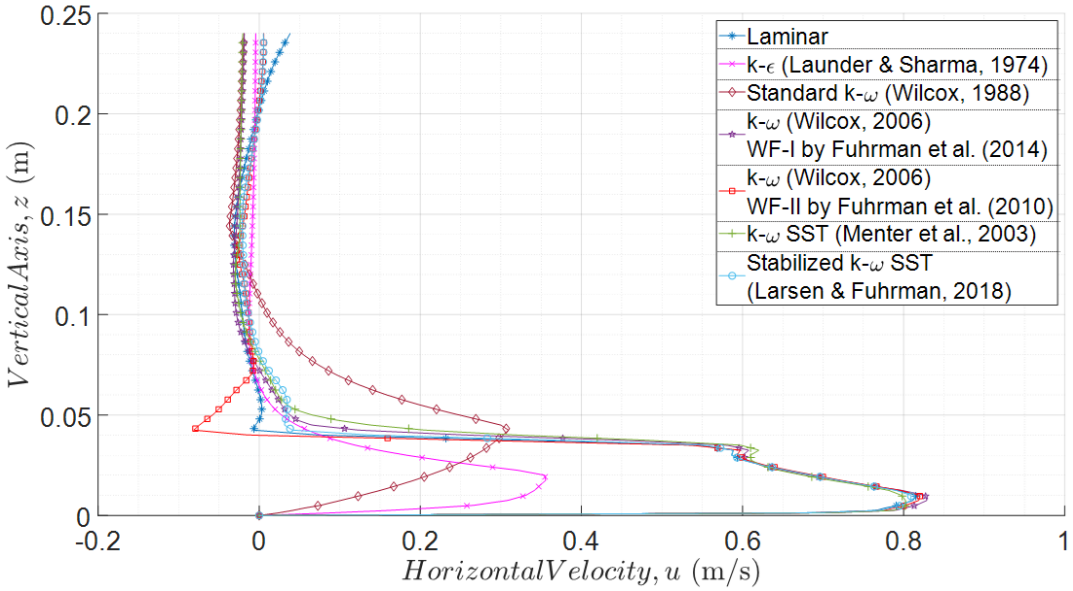

Figure 4.6: Vertical variation of horizontal velocity (u) for H=8.6 cm

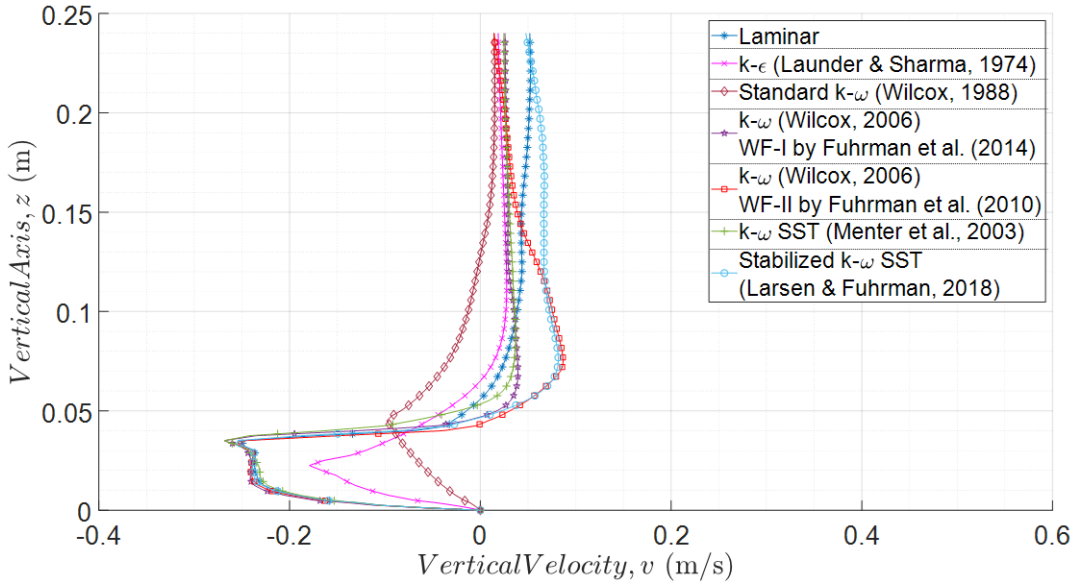

Figure 4.7: Vertical variation of vertical velocity (v) for H=8.6 cm

In Figure 4.6 and Figure 4.7, it can be seen that stabilized k-ω SST, k-ω SST, k-ω, and laminar results show similar peak values at the top of the crown wall. In contrast, k-ε and standard k-ω turbulence models show lower absolute velocity magnitudes compared to the other models, which is a consequence of the overproduction of turbulent kinetic energies and high eddy viscosities. In terms of the horizontal velocities, both k-ε and standard k-ω turbulence models show similar peak values. On the other hand, the peak value of the vertical velocity of the standard k-ω turbulence model is two times higher than the one for the k-ε turbulence model. The over-predicted jet thicknesses and the longer overtopping durations can be explained by high vertical velocities produced by the standard k-ω turbulence model.

4.2 Morphological Results

In this part, the numerical results of the morphological simulations are compared with the experimental results obtained by Yaman (2022). Furthermore, the performances of different turbulence model and wall function couplings on the morphological changes are evaluated. In the first part of this section, bed profiles obtained from the numerical simulations are compared with the experimental results,

and the effects of turbulence models and the wall functions are discussed. Then, the scour hole properties are discussed in terms of the depth and length of the scour hole and the distance of the deepest point to the crown wall. Finally, maximum Shields parameters at the bottom are calculated and compared for different turbulence model and wall function couplings.

4.2.1 Bed Profiles

During the simulations, bed morphology is updated until the wave overtopping is finished. Then, the bottom elevations are determined and compared with the experimental result. Furthermore, it is noted that the scour profiles are non-dimensionalized by dividing the scour depth by the grain diameter. In Figure 4.8, a comparison of non-dimensional scour profiles for MD01, MD04, MD06, and MD07 (H=8.6 cm) is given. It should be noted that the results of k-ε, standard k-ω, and k-ω *WF-II* simulations are not presented since the over-produced turbulent parameters introduce unphysical deformations resulting in instability problems in the model.

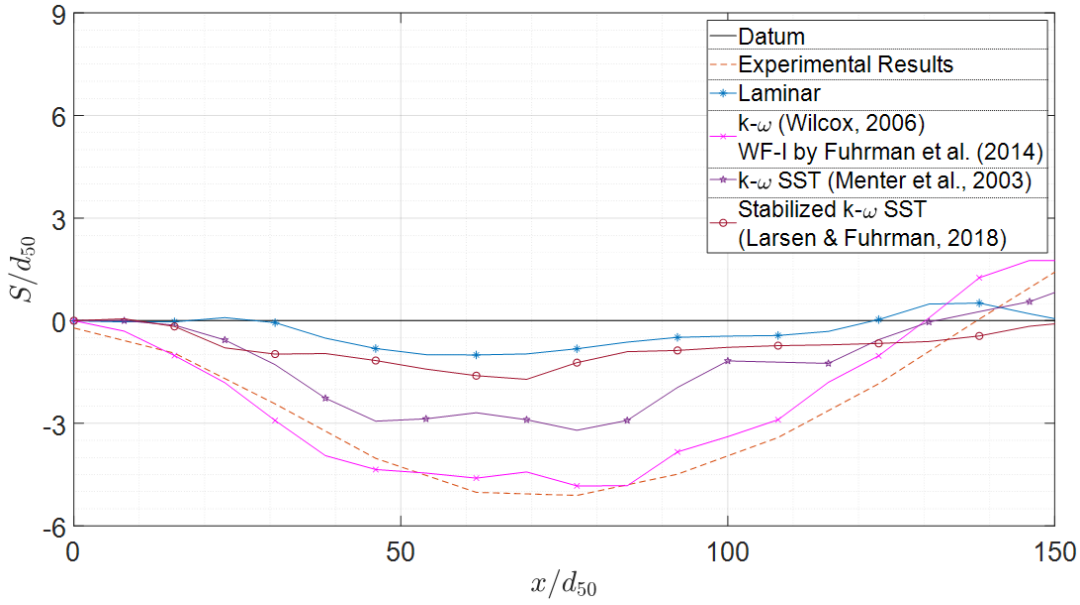

Figure 4.8: Comparison of scour profiles for H=8.6 cm

As stated previously, *k-ε*, standard *k-ω*, and *k-ω WF-II* simulation results are not presented in Figure 4.8 due to the stability problems of the model. The reason behind this issue is the overproduction of the turbulent kinetic energy and the eddy viscosity values. Consequently, the sediment transport rates are increased significantly, and the vertex points of the bottom cells are deformed unphysically. As a result, the non-orthogonality increases while the mesh quality decreases, which causes stability problems during the simulations. This issue is further presented and explained in the next paragraphs. It should also be noted that *k-ε* and standard *k-ω* simulations showed poor hydrodynamic results and transferred high turbulent kinetic energies to the morphological part.

In Figure 4.8, it is observed that the *k-ω* (Wilcox, 2006) simulation with the wall functions by Fuhrman et al. (2014) shows the best agreement with the experimental results in terms of the scour profile. In the literature, this turbulence model and the wall function are successfully used by several studies to investigate the scour around the piles and the scour beneath the pipelines (Baykal et al., 2014; Baykal et al., 2015; Baykal et al. 2017). Similarly, they also worked well to estimate the scour profile at the rear side of a rubble mound coastal revetment due to the overtopping of solitary-like waves. On the other hand, *k-ω* (Wilcox, 2006) simulation with the wall functions by Fuhrman et al. (2010) shows the unphysical bottom elevation changes. Although the turbulence models are similar, using different wall functions affected the morphological results significantly as the sediment transport is highly related to the near-wall region behavior. It is also interesting to note that *k-ω WF-II* simulations show similar results to *k-ω WF-I* simulation results during the hydrodynamic studies (Figure 4.1). On the other hand, there is a severe difference between the bottom elevations as the wall functions play an essential role in determining the scour profiles.

As expected, the laminar simulation result is smaller than the other ones since there is not any effect of turbulence on this simulation (Figure 4.8). As stated by Sumer et al. (2003), turbulence is a vital parameter to enhance the sediment transport rates.

Therefore, the simulations that do not use a turbulence model might get a smaller scour profile than the others. It should also be noted that the hydrodynamic performance of the laminar simulation was good, and the results were analogous to the stabilized k-ω SST, k-ω SST, and k-ω simulations. On the other hand, the scour profile is underestimated when laminar theory is used, showing the turbulence's importance on sediment transport. Nevertheless, the laminar simulation does not introduce stability problems due to high deformations.

In Figure 4.8, it is observed that the k-ω *WF-I* simulation shows a better agreement than the k-ω SST simulation. On the other hand, these simulations showed similar results in the hydrodynamic studies in terms of both the free surface elevations and the turbulence parameters. Furthermore, Baykal et al. (2017) stated that the k-ω turbulence model shows a similar level of accuracy with the k-ω SST turbulence model for morphological studies. In this study, there was a moderate difference between these simulations. The reason behind this is probably the use of different wall functions.

An interesting result obtained from Figure 4.8 is that the stabilized k-ω SST simulation shows a similar scour profile to the laminar simulation. The first reason behind this issue might be the wall function that is used. The second one might be the transmission of lower turbulent parameters due to the buoyancy production term. This issue is further discussed in the next paragraphs.

Furthermore, the k-ω SST simulation shows a better agreement than the stabilized k-ω SST simulation. Although the same wall functions are used for both simulations, using a different turbulence model affected the morphological results significantly. To further investigate this issue, turbulent kinetic energy and eddy viscosity distributions taken from the same time are presented in the following figures.

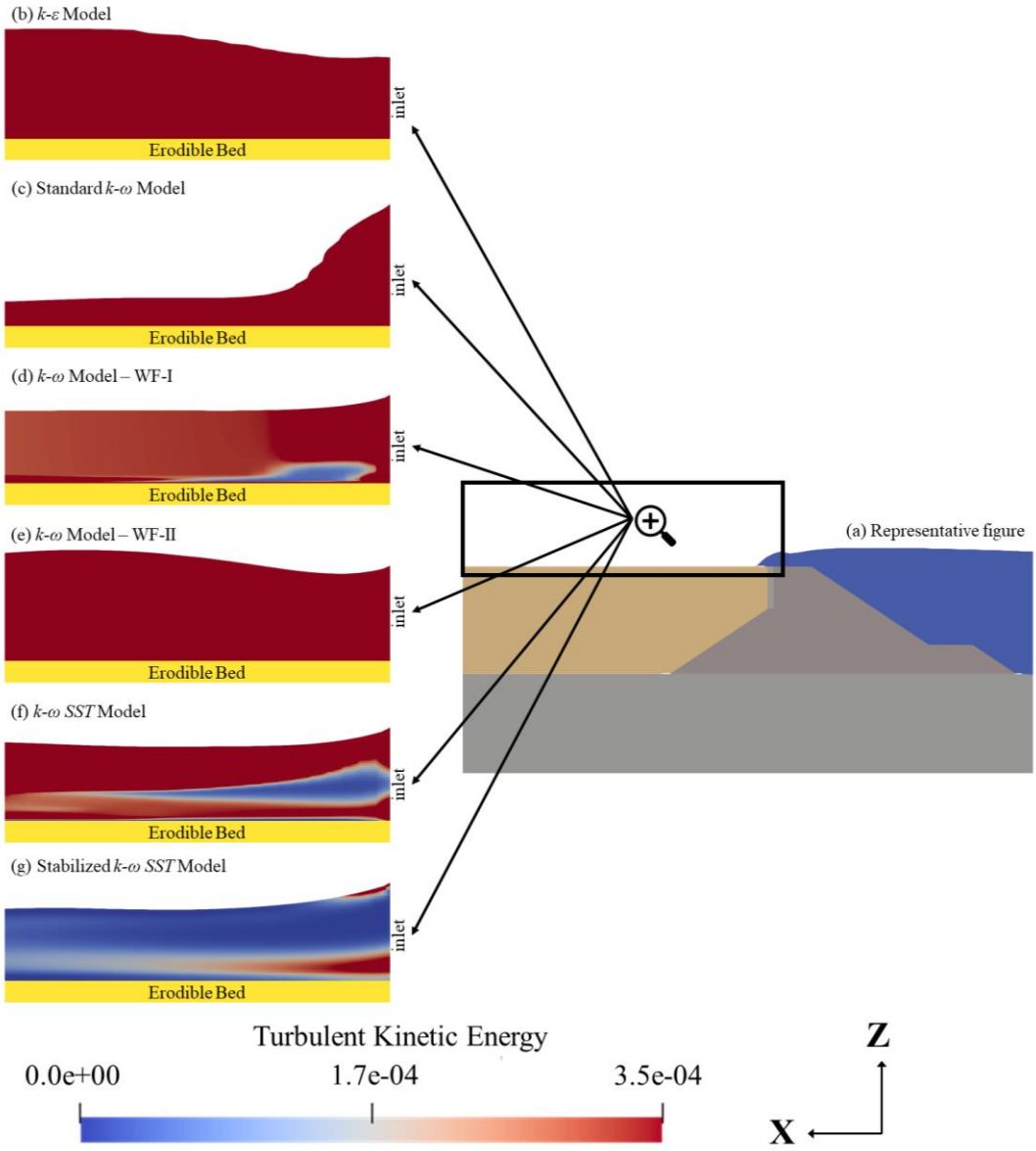

Figure 4.9. Turbulent kinetic energy (m^2/s^2) snapshots for H=8.6 cm, (a) Representative figure, (b) *k-ε*, (c) Standard *k-ω*, (d) *k-ω WF-I*, (e) *k-ω WF-II*, (f) *k-ω SST*, (g) Stabilized *k-ω SST*

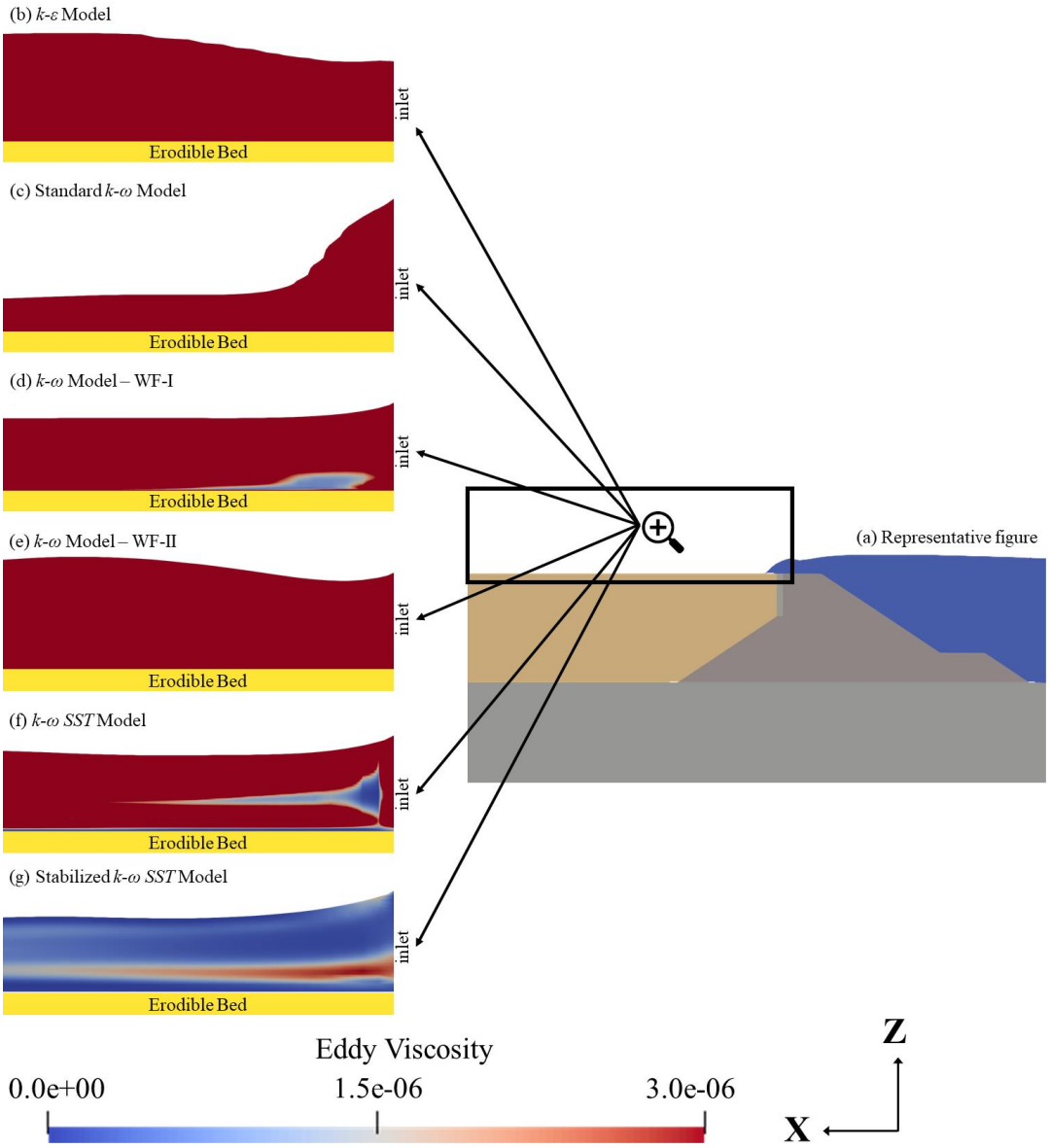

Figure 4.10. Eddy viscosity (m^2/s) snapshots for H=8.6 cm, (a) Representative figure (b) *k-ε*, (c) Standard *k-ω*, (d) *k-ω WF-I*, (e) *k-ω WF-II*, (f) *k-ω SST*, (g) Stabilized *k-ω SST*

In Figure 4.9 and Figure 4.10, it can be seen that k-ε, standard k-ω, and k-ω *WF-II* simulations yield high turbulent kinetic energy and eddy viscosity values. Therefore, the sediment transport rates are enhanced due to the high turbulent parameters, and the unphysical bottom elevation changes are observed. It should also be noted that the transferred turbulent parameters from the hydrodynamic studies to morphological studies are also high in k-ε and standard k-ω simulations. On the other hand, the transferred turbulent parameters of k-ω *WF-II* simulation are similar to k-ω *WF-I* simulation. Although the inputs are similar and the turbulence models are analogous to each other, using a different wall function yields unphysical turbulent parameters, resulting in high deformations in the mesh. Consequently, stability problems are introduced in the model due to the high non-orthogonality values in the bottom cells.

Another interesting observation from Figure 4.9 and Figure 4.10 is that the free surface profiles of k-ε, standard k-ω, and k-ω *WF-II* simulations are different from the other simulations. Furthermore, it is observed from the laboratory video records provided by Yildirim (2021) and Yaman (2022) that the free surface profile is analogous to the k-ω *WF-I*, k-ω *SST*, and stabilized k-ω *SST* simulation results. For standard k-ω simulation, a higher water column thickness is observed at the beginning of the domain due to the high jet thickness values, as expressed in Table 4.3. However, the thickness significantly decreases when it goes away from the inlet. One reason behind this issue might be the low horizontal velocity values (Figure 4.6). Another reason might be the high turbulent kinetic energy values that consume the total energy. On the other hand, k-ε and k-ω *WF-II* simulations show similar free surface profiles where the water column thickness is increased away from the inlet. This issue is left to be studied in the future as a further study.

As expressed previously, the k-ω *WF-I* simulation shows the best agreement with the experimental results in terms of the scour profile, while the k-ω *SST* model is the second-best (Figure 4.8). Although the hydrodynamic results of these turbulence models are similar to each other, there is a moderate difference between the scour

profiles. Figure 4.9 and Figure 4.10 show that the main difference between the models in the morphological studies is the turbulent kinetic energy and the eddy viscosity values near the wall. It is observed in Figure 4.9 (c) and Figure 4.10 (c) that the turbulent kinetic energy and the eddy viscosity values for *k-ω WF-I* simulation are higher than the ones for *k-ω SST* simulation near the wall. On the other hand, these values are similar to each other above the wall region. The primary reason behind this is probably the use of different wall functions since the boundary conditions used for the turbulent parameters significantly affect the near-wall behavior. Because turbulence is an essential factor that enhances the sediment transport rates, the *k-ω WF-I* simulation result shows about %40 deeper scour profile than the *k-ω SST* simulation, which also matches the experimental results best.

In addition, Figure 4.9 and Figure 4.10 show that there is a significant inequality regarding the turbulent parameters for *k-ω SST* and stabilized *k-ω SST* simulation results in the morphological studies. Furthermore, it should be noted that a similar difference is also presented in the hydrodynamic simulations (Figure 4.2 and Figure 4.3). In both hydrodynamic and morphological studies, it is observed that using a buoyancy production term in the stabilized *k-ω SST* simulations decreases the turbulent kinetic energy values significantly near the free surface region. Therefore, both the transferred and the generated turbulent parameters for the stabilized *k-ω SST* simulation are smaller than those for *k-ω SST* simulation. Consequently, the depth of the scour hole of the *k-ω SST* simulation is about 2 times larger than the stabilized *k-ω SST*. It is also observed both turbulence models show relatively small turbulent parameters near the wall region compared to *k-ω WF-I* simulation since they use the same wall function. Yet, *k-ω SST* simulation shows a larger scour hole due to the higher transferred and generated turbulent parameters.

4.2.2 Scour Hole Properties

In this part of the study, non-dimensional scour hole properties are calculated and compared with the experimental results. In Table 4.5, the depth of the scour hole (*S*),

length of the scour hole (L), and the distance of the deepest point to the crown wall (X_s) are given in non-dimensional forms for MD01, MD04, MD06, and MD07 (H=8.6 cm) simulations. Furthermore, a mean absolute percentage error (MAPE) methodology is used to measure the accuracy of the turbulence models to predict the scour hole dimensions. MAPE values are also given in Table 4.5.

Table 4.5 Scour hole properties

	Dimensions			**MAPE**		
	***S/d*$_{50}$**	***L/d*$_{50}$**	***X*$_s$*/d*$_{50}$**	***S/d50***	***L/d*$_{50}$**	***X*$_s$*/d*$_{50}$**
Experimental Result	5.1	138.1	78.8	-	-	-
Laminar	1.0	123.3	61.1	80.4	10.7	22.5
k-ω WF-I	4.9	130.8	82.2	3.9	5.3	4.3
k-ω SST	3.3	131.2	76.0	35.3	5.0	3.6
Stabilized *k-ω SST*	1.7	153.2	69.7	66.7	10.9	11.5

In Table 4.5, it is observed that the *k-ω WF-I* simulation shows the best agreement with the experimental result in terms of the scour depth. Furthermore, *k-ω SST* simulation also gives fair scour depth results, while laminar and stabilized *k-ω SST* simulations show poor ones. The reasons behind this issue are further discussed in the previous section. On the other hand, all simulations show good agreements with the experimental results regarding the length of the scour hole. The reason why all simulations show accurate results to predict the scour length is left as a further discussion topic. Furthermore, *k-ω SST* and *k-ω WF-I* simulations match well with the experimental data in terms of the distance of the deepest point to the crown wall. Stabilized *k-ω SST* simulation, on the other hand, shows an acceptable performance to determine X_s/d_{50} while the laminar simulation does not.

In Table 4.5, it is observed that scour length and distance from the crown wall parameters are captured by *k-ω SST* simulation as accurately as *k-ω WF-I* simulation. On the other hand, there is a moderate difference between these simulations regarding the scour depth. In conclusion, the *k-ω SST* turbulence model

can also be used to simulate the scour at the rear side of a coastal revetment by recognizing that the scour depth is under-predicted if *k-ω WF-I* is not available somehow.

4.2.3 Shields Parameters

According to Soulsby (1997), the Shields parameter (θ) can be described as a non-dimensional form of the bed shear stress. Furthermore, it is an important parameter that controls the initiation of the sediment motion under a flow. In this part of the study, maximum Shields parameters for MD01, MD04, MD06, and MD07 (H=8.6 cm) simulations are calculated and compared in Figure 4.11.

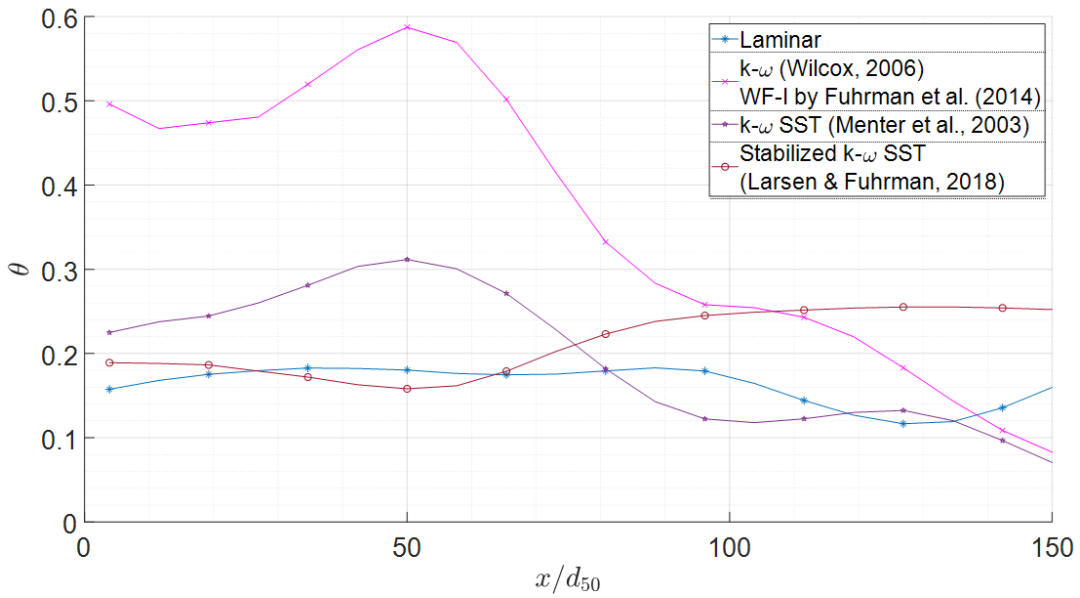

Figure 4.11. Maximum Shields parameters (θ)

In Figure 4.11, the maximum Shields parameters for all simulations are much higher than the critical Shields parameter, which is taken as 0.045 in this study. Furthermore, according to Celik and Rodi (1991), the critical threshold value for sediment suspension is determined as 0.25. As it can be seen from Figure 4.11, *k-ω WF-I*, and *k-ω SST* simulations exceeds the threshold value, consequently, the suspended sediment transport is initiated. On the other hand, Shields parameters for

the stabilized *k-ω SST* and laminar simulations are computed as about 0.20 which is not enough for the initiation of the suspended sediment transport. It is also observed from Figure 4.8 that the scour profiles of *k-ω WF-I* and *k-ω SST* simulations match better with the experimental result than the other simulations. For this reason, it can be stated that the sediment suspension is needed to be computed accurately to obtain a realistic scour profile. It is also known that the suspended sediment transport rates are increased when the Shields parameter rises. Therefore, it can be concluded that the suspended sediment transport is a significant contributor to the scour process.

In Figure 4.11, the *k-ω WF-I* simulation shows much higher Shields parameters than the other simulations as it gives the deepest scour profile presented in Figure 4.8. Furthermore, Shields parameters obtained from the *k-ω SST* simulation are about %50 lower than those for the *k-ω WF-I* simulation, but they are about %40 higher than the other results. Moreover, these results show a good agreement with the ones presented in Figure 4.8.

An interesting result observed from Figure 4.11 is that the Shields parameters for stabilized *k-ω SST* and laminar simulations are similar to each other near the inlet. However, the laminar simulation shows a slight drop at about x/d_{50}=70, while the stabilized *k-ω SST* simulation shows a gradual increase followed by a leveling off at the same position. This issue is also matched well with the scour length results presented in Table 4.5. In the previous section, it is stated that the scour length obtained from the stabilized *k-ω SST* simulation is higher than the one for the laminar simulation. In addition, Shields parameter results presented in Figure 4.11 also show that the drop in the Shields parameter is postponed for stabilized *k-ω SST* simulation, resulting in a higher scour length compared to the laminar simulation. On the other hand, *k-ω WF-I* and *k-ω SST* simulations show dramatic falls at about x/d_{50}=60, and Shields parameters become similar to each other when x/d_{50}=140. This issue also explains the similarity of the scour lengths between *k-ω WF-I* and *k-ω SST* simulations.

CHAPTER 5

CONCLUSIONS AND FURTHER STUDIES

The primary purpose of this thesis study is to evaluate the performances of different turbulence model and wall function couplings in hydrodynamic and morphological studies. To investigate it, a coupled hydrodynamic and morphological CFD model is used. In the first part of this study, hydrodynamic simulations are carried on, and the results are compared with the experimental data. Furthermore, the effects of using different turbulence model and wall function couplings on the hydrodynamic results are investigated. In the second part, morphological simulations are studied, and the bed elevation results are discussed with the turbulent parameters. The significant findings of this thesis study are itemized below:

- Porous media friction coefficients for a solitary-like wave – rubble mound coastal revetment interaction are calibrated as α=10 and β=0.6 for the armor layer, α=20 and β=0.7 for the filter layer, α=10 and β=0.5 for the core layer, and α=10 and β=0.5 for the backfill material. Furthermore, the added mass coefficient (C) is chosen as 0.34.
- In the hydrodynamic studies, it is observed that there is not a significant effect of using different wall functions on the hydrodynamic results since the free surface behavior is not directly related to the near-wall region behavior.
- Hydrodynamic results showed that the laminar, k-ω (Wilcox, 2006), k-ω SST (Menter et al., 2003), and stabilized k-ω SST (Larsen and Fuhrman, 2018) turbulence models show good agreements with the experimental data. On the other hand, k-ε (Launder and Sharma, 1974) and standard k-ω (Wilcox, 1988) turbulence models show poor estimations due to the over-produced turbulent parameters.
- Turbulent kinetic energy and eddy viscosity values that are obtained from the hydrodynamic simulations of k-ω (Wilcox, 2006) and k-ω SST (Menter et

al., 2003) turbulence models are similar to each other. On the other hand, stabilized k-ω SST (Larsen and Fuhrman, 2018) turbulence model reduces the turbulent parameters near the free surface region mainly due to the buoyancy production term.

- In the morphological studies, it is observed that the k-ω (Wilcox, 2006) turbulence model combined with Fuhrman et al. (2014) wall functions shows the best agreement with the experimental results to predict the scour profile. Next, k-ω SST (Menter et al., 2003) turbulence model with the default wall functions comes second.
- Morphological simulations showed that the use of different wall functions affects the scour profile results significantly since the near-wall behavior is a major contributor to the sediment transport phenomenon. Furthermore, it is observed that the use of Fuhrman et al. (2014) wall functions shows the best results.
- To predict the scour length and the distance of the deepest point to the crown wall, laminar, k-ω SST (Menter et al., 2003), stabilized k-ω SST (Larsen and Fuhrman, 2018) and k-ω (Wilcox, 2006) with the wall functions presented by Fuhrman et al. (2014) simulations show good agreements, although the scour depths are quite different from each other.
- It is observed that the suspended sediment transport is needed to be predicted accurately to obtain a realistic scour profile since it affects the scour rate considerably.

This study's primary purpose is to evaluate the performances of different turbulence model and wall function couplings in hydrodynamic and morphological simulations for a specific condition. In this context, a rubble mound coastal revetment under a solitary-like wave attack is considered. Furthermore, the rear side of the structure is filled with a non-cohesive bed material such that the elevations of the crown wall and the rear side are the same. Although the simulations are carried on for the given circumstances, it is planned to extend the study for further investigations by changing the existing conditions. In addition, it is also planned to develop the model further

so that the computational time can be reduced. Further studies, future recommendations, and major drawbacks of the study are itemized below:

- In this study, overtopping of solitary-like waves is considered. On the other hand, overtopping of regular and irregular waves might cause a different flow condition at the rear side since the individual overtopping volume is much lower than a solitary wave overtopping volume. Therefore, this study is planned to be extended to investigate the effects of turbulence models and wall functions under regular and irregular wave attacks.
- Another future study is to investigate the effects of dynamic pressures on the scour profiles by increasing the elevation of the crown wall. Therefore, the overtopping jet flows can hit the backfill material with higher vertical velocities, which results in higher pressure values.
- Same simulations can be carried on by changing the type of the backfill material to investigate the effects of boundary layer thickness and sand roughness. Furthermore, the rear side of the coastal revetment can be filled with asphalt or concrete to extend the study for practical applications.
- In the hydrodynamic part of this study, different wave heights are studied. However, some of these results are not further used in the morphological simulations due to the high computational demand of the model. As a future study, the effects of different wave heights on the morphological results can be investigated.
- Although RANS models are compared in this study, there are several advanced turbulence models in the literature, such as large eddy simulation (LES), direct numerical simulation (DNS), and Reynolds stress equation model (RSM). In future studies, the performance of these turbulence models can be investigated.
- As discussed previously, the high computational time is a major drawback of this study. Most OpenFOAM distributors have been trying to speed up the code for faster and more stable simulations. In this study, one of the former versions of OpenFOAM is used since the model is developed in this library.

The author has modified and implemented the model to a recent version of OpenFOAM (FOAM-Extend 3.1). However, the validation study has not been completed yet. When the recent model is validated, it is expected to carry out more stable and faster simulations.

- In this study, simulations are done in two steps: hydrodynamic and morphological parts. The major reasons behind this issue are explained previously. On the other hand, the author has attempted to modify and develop the solver to carry on these studies in a single simulation. In the solver, porous media equations and free surface capturing algorithms are added, and a switch keyword is implemented such that the morphological studies can be stopped entirely for the given time. However, the solver has not been validated yet. When the validation studies are completed, studies can be carried on in a single simulation.

REFERENCES

Amiraslani, S., Fahimi, J., & Mehdinezhad, H. (2010, December 6-8). *The Numerical Investigation of Free Falling Jet's Effect on the Scour of Plunge Pools* [Paper presentation]. XVIII International Conference on Water Resources, Riyadh, Saudi Arabia.

Arikawa, T., Akiyama, M., & Yamazaki, N. (2011). Development of Solid-Gas-Liquid Coupling System by using CADMAS-SURF/3D. *Journal of Japan Society of Civil Engineers, Ser. B2 (Coastal Engineering)*, *67*(2), I_21-I_25.

Bardina, J. E., Huang, P. G., & Coakley, T. J. (1997). *Turbulence modeling validation, testing and development*, NASA Technical Memorandum 110446.

Baykal, C., Sumer, B. M., Fuhrman, D. R., Jacobsen, N. G., & Fredsoe, J. (2014). Numerical Modeling of Backfilling Process Around Monopiles. *Coastal Engineering Proceedings*, *1*(34), 22. https://doi.org/10.9753/icce.v34.sediment.22

Baykal, C., Sumer, B. M., Fuhrman, D. R., Jacobsen, N. G., & Fredsoe, J. (2015). Numerical investigation of flow and scour around a vertical circular cylinder. *Philosophical Transactions of the Royal Society A: Mathematical, Physical and Engineering Sciences*, *373*(2033), 20140104. https://doi.org/10.1098/rsta.2014.0104

Baykal, C., Sumer, B. M., Fuhrman, D. R., Jacobsen, N. G., & Fredsøe, J. (2017). Numerical simulation of scour and backfilling processes around a circular pile in waves. *Coastal Engineering*, *122*, 87–107. https://doi.org/10.1016/j.coastaleng.2017.01.004

Bazilevs, Y., Hsu, M., Kiendl, J., Wüchner, R., & Bletzinger, K. (2011). 3D Simulation of Wind Turbine Rotors at Full Scale. Part II: Fluid – Structure Interaction Modeling with Composite Blades. *International Journal for Numerical Methods in Fluids*, *65*, 236–253. https://doi.org/10.1002/fld

Beattie, J., & Kriel, N. (2019). Is The Starry Night Turbulent?. arXiv:1902.03381

Berberovic, E., van Hinsberg, N., Jakirlic, S., Roisman, I. & Tropea, C. (2009). Drop Impact onto a Liquid Layer of Finite Thickness: Dynamics of the Cavity Evolution, *Physical Review E*, *79*(3). https://doi.org/10.1103/physreve.79.036306

Bomers, A., Aguilar Lopez, J. P., Warmink, J. J., & Hulscher, S. J. M. H. (2018). Modelling effects of an asphalt road at a dike crest on dike cover erosion onset during wave overtopping. *Natural Hazards*, *93*(1), 1–30. https://doi.org/10.1007/s11069-018-3287-y

Caliskan, U., & Fuhrman, D. R. (2017). RANS-based simulation of wave-induced sheet-flow transport of graded sediments. *Coastal Engineering*, *121*, 90–102. https://doi.org/10.1016/j.coastaleng.2016.11.007

Castillo, L. G., Castro, M., Carrillo, J. M., Hermosa, D., Hidalgo, X., & Ortega, P. (2016). Experimental and numerical study of scour downstream Toachi Dam. *Sustainable Hydraulics in the Era of Global Change - Proceedings of the 4th European Congress of the International Association of Hydroenvironment Engineering and Research, IAHR 2016*, 519–526.

Cebeci, T., & Chang, K. C. (1978). Calculation of incompressible rough-wall boundary-layer flows. *AIAA Journal*, *16*(7), 740–746.

Celik, I., & Rodi, W. (1991). Suspended Sediment-Transport Capacity for Open Channel Flow. *Journal of Hydraulic Engineering*, *117*(2), 191–204. https://doi.org/10.1061/(asce)0733-9429(1991)117:2(191)

Chen, W., Warmink, J. J., van Gent, M. R. A., & Hulscher, S. J. M. H. (2021). Numerical modelling of wave overtopping at dikes using OpenFOAM®. *Coastal Engineering*, *166*, 103890.

Cheng, Z., Hsu, T. J., & Calantoni, J. (2017). SedFoam: A multi-dimensional Eulerian two-phase model for sediment transport and its application to momentary bed failure. *Coastal Engineering*, *119*, 32–50.

Davanipour, M., Javanmardi, H., & Goodarzi, N. (2018). Chaotic Self-Tuning PID Controller Based on Fuzzy Wavelet Neural Network Model. *Iranian Journal of Science and Technology - Transactions of Electrical Engineering*, *42*(3), 357–366. https://doi.org/10.1007/s40998-018-0069-1

Dean, R. G., & Dalrymple, R. A. (1991). *Water wave mechanics for engineers and scientists.* World scientific

Deissler, R. G. (1955). *Analysis of Turbulent Heat Transfer, Mass Transfer and Friction in Smooth Tubes at High Prandtl ajid Schmidt Numbers*, NACA Tech. Note 3145.

del Jesus, M., Lara, J. L., & Losada, I. J. (2012). Three-dimensional interaction of waves and porous coastal structures. Part I: Numerical model formulation. *Coastal Engineering*, *64*, 57–72. https://doi.org/10.1016/j.coastaleng.2012.01.008

Deshpande, S. S., Anumolu, L., & Trujillo, M. F. (2012). Evaluating the performance of the two-phase flow solver interFoam. *Computational Science and Discovery*, *5*(1). https://doi.org/10.1088/1749-4699/5/1/014016

Devolder, B., Troch, P., & Rauwoens, P. (2018). Performance of a buoyancy-modified k-ω and k-ω SST turbulence model for simulating wave breaking under regular waves using OpenFOAM®. *Coastal Engineering*, *138*, 49–65. https://doi.org/10.1016/j.coastaleng.2018.04.011

Dodd, N., (1998). Numerical Model of Wave Run-Up, Overtopping, and Regeneration. *Journal of Waterway, Port, Coastal, and Ocean Engineering*, *124*(2), 73–81.

Einstein, A. H. (1950). The Bed-Load Function for Sediment Transportation in Open Channel Flows. *Technical Bulleting*, *1026*(1026). https://naldc.nal.usda.gov/download/CAT86201017/PDF

Engelund, F., & Fredsøe, J. (1976). A Sediment Transport Model for Straight Alluvial Channels. *Hydrology Research*, *7*(5), 293–306. https://doi.org/10.2166/nh.1976.0019

Eurotop. (2018). *Eurotop 2018; Manual on wave overtopping of sea defences and related structures. An overtopping manual largely based on European research, but for worldwide application.* 320. www.overtopping-manual.com

Fenton, J. D. (1988). The numerical solution of steady water wave problems. *Computers and Geosciences*, *14*(3), 357–368. https://doi.org/10.1016/0098-3004(88)90066-0

Ferziger, J. H., Perić, M., & Street, R. L. (2019). *Computational Methods for Fluid Dynamics* (4th ed. 2020 ed.). Springer.

Fredsoe, J., & Deigaard, R. (1992). *Mechanics of Coastal Sediment Transport (Advanced Ocean Engineering).* World scientific.

Fuhrman, D. R., Baykal, C., Mutlu Sumer, B., Jacobsen, N. G., & Fredsøe, J. (2014). Numerical simulation of wave-induced scour and backfilling processes beneath submarine pipelines. *Coastal Engineering*, *94*, 10–22. https://doi.org/10.1016/j.coastaleng.2014.08.009

Fuhrman, D. R., Dixen, M., & Jacobsen, N. G. (2010). Physically-consistent wall boundary conditions for the k-turbulence model. *Journal of Hydraulic Research*, *48*(6), 793–800. https://doi.org/10.1080/00221686.2010.531100

Fuhrman, D. R., Schløer, S., & Sterner, J. (2013). RANS-based simulation of turbulent wave boundary layer and sheet-flow sediment transport processes. *Coastal Engineering*, *73*, 151–166. https://doi.org/10.1016/j.coastaleng.2012.11.001

Guler, H. G., (2020).Numerical Modelling of Wave-Structure Interaction Problems Through CFD Methods. *Ph.D. Thesis*, Middle East Technical University.

Guler, H. G., Baykal, C., Arikawa, T., & Yalciner, A. C. (2018). Numerical assessment of tsunami attack on a rubble mound breakwater using

OpenFOAM®. *Applied Ocean Research*, *72*, 76–91. https://doi.org/10.1016/j.apor.2018.01.005

Higuera, P. (2015). Application of computational fluid dynamics to wave action on structures. *Ph.D. Thesis*, 1–356. http://www.tesisenred.net/handle/10803/288368

Higuera, P., Lara, J. L., & Losada, I. J. (2013). Realistic wave generation and active wave absorption for Navier-Stokes models. Application to OpenFOAM®. *Coastal Engineering*, *71*, 102–118. https://doi.org/10.1016/j.coastaleng.2012.07.002

Higuera, P., Lara, J. L., & Losada, I. J. (2014a). Three-dimensional interaction of waves and porous coastal structures using OpenFOAM®. Part I: Formulation and validation. *Coastal Engineering*, *83*, 243–258. https://doi.org/10.1016/j.coastaleng.2013.08.010

Higuera, P., Lara, J. L., & Losada, I. J. (2014b). Three-dimensional interaction of waves and porous coastal structures using OpenFOAM®. Part II: Application. *Coastal Engineering*, *83*, 259–270. https://doi.org/10.1016/j.coastaleng.2013.09.002

Hirt, C. W. & Nichols, B. D. (1981). Volume of Fluid (VOF) Method for the Dynamics of Free Boundaries. *Journal of Computational Physics*, *39*, 201–225.

Hsiao, S. C., & Lin, T. C. (2010). Tsunami-like solitary waves impinging and overtopping an impermeable seawall: Experiment and RANS modeling. *Coastal Engineering*, *57*(1), 1–18. https://doi.org/10.1016/j.coastaleng.2009.08.004

Hu, K., Mingham, C., & Causon, D. (2000). Numerical simulation of wave overtopping of coastal structures using the non-linear shallow water equations. *Coastal Engineering*, *41*(4), 433–465. https://doi.org/10.1016/s0378-3839(00)00040-5

Hubbard, M. E., & Dodd, N. (2002). A 2D numerical model of wave run-up and

overtopping. *Coastal Engineering*, *47*(1), 1–26. https://doi.org/10.1016/S0378-3839(02)00094-7

Hudson, R. Y., Hermann, F. A., Sager, R. A., Whalin, R. W., Keulegan, G. H., Chatnam, C. E., & Hales, L. Z. (1979). *Coastal hydraulic models*. Special Report No: 5 US Army Engineer Waterways Experiment Station

Jacobsen, N. G., Fuhrman, D. R., & Fredsoe, J. (2012). A Wave Generation Toolbox for the Open-Source CFD Library: OpenFOAM®. *International Journal for Numerical Methods in Fluids*, *70*(9)1073-1088.

Jacobsen, Niels G., Fredsoe, J., & Jensen, J. H. (2014). Formation and development of a breaker bar under regular waves. Part 1: Model description and hydrodynamics. *Coastal Engineering*, *88*, 182–193. https://doi.org/10.1016/j.coastaleng.2013.12.008

Jacobsen, Niels Gjøl. (2011). A Full Hydro- and Morphodynamic Description of Breaker Bar Development. *Ph.D. Thesis*, *April*, 200.

Jayaratne, R., Abimola, A., Mikami, T., Matsuba, S., Esteban, M., & Shibayama, T. (2014). Predictive Model for Scour Depth of Coastal Structure Failures Due To Tsunamis. *Coastal Engineering Proceedings*, *1*(34), 56. https://doi.org/10.9753/icce.v34.structures.56

Jensen, B., Jacobsen, N. G., & Christensen, E. D. (2014). Investigations on the porous media equations and resistance coefficients for coastal structures. *Coastal Engineering*, *84*, 56–72. https://doi.org/10.1016/j.coastaleng.2013.11.004

Jiménez, J. (2006). The numerical computation of turbulence. *Lecture Notes On Turbulence And Coherent Structures In Fluids, Plasmas And Nonlinear Media*, 281–307. https://doi.org/10.1142/9789812774071_0006

Kalitzin, G., Medic, G., Iaccarino, G., & Durbin, P. (2005). Near-wall behavior of RANS turbulence models and implications for wall functions. *Journal of*

Computational Physics, *204*(1), 265–291. https://doi.org/10.1016/j.jcp.2004.10.018

Launder, B. E., & Sharma, B. I. (1974). Application of the Energy-Dissipation Models of Turbulence to the Calculation of Flow Near a Spinning Disc. *Letters in Heat and Mass Transfer*, 131–138.

Larsen, B. E., & Fuhrman, D. R. (2018). On the over-production of turbulence beneath surface waves in Reynolds-averaged Navier-Stokes models. *Journal of Fluid Mechanics*, *853*, 419–460. https://doi.org/10.1017/jfm.2018.577

Larsen, B. E., Fuhrman, D. R., & Roenby, J. (2019). Performance of interFoam on the simulation of progressive waves. *Coastal Engineering Journal*, *61*(3), 380–400. https://doi.org/10.1080/21664250.2019.1609713

Lee, J. J., Skjelbreia, E., & Raichlen, F. (1982). Measurement of Velocities in Solitary Waves. *Journal of Waterway, Port, Coastal, and Ocean Engineering*, *108*(2), 200–218

Li, J., Fuhrman, D. R., Kong, X., Xie, M., & Yang, Y. (2021). Three-dimensional numerical simulation of wave-induced scour around a pile on a sloping beach. *Ocean Engineering*, *233*, 109174. https://doi.org/10.1016/j.oceaneng.2021.109174

Liu, F. (2016). Thorough Description of How Wall Functions Are Implemented in OpenFOAM. *In Proceedings of CFD with OpenSource Software*, 1–30.

Losada, I. J., Lara, J. L., & del Jesus, M. (2016). Modeling the Interaction of Water Waves with Porous Coastal Structures. *Journal of Waterway, Port, Coastal, and Ocean Engineering*, *142*(6), 03116003. https://doi.org/10.1061/(asce)ww.1943-5460.0000361

Losada, I. J., Lara, J. L., Guanche, R., & Gonzalez-Ondina, J. M. (2008). Numerical analysis of wave overtopping of rubble mound breakwaters. *Coastal Engineering*, *55*(1), 47–62. https://doi.org/10.1016/j.coastaleng.2007.06.003

Marusic, I., & Broomhall, S. (2021). Leonardo da Vinci and Fluid Mechanics. *Annual Review of Fluid Mechanics*, *53*, 1–25. https://doi.org/10.1146/annurev-fluid-022620-122816

Mayer, S., & Madsen, P. A. (2000). Simulation of breaking waves in the surf zone using a Navier-Stokes solver. *Coastal Engineering 2000 - Proceedings of the 27th International Conference on Coastal Engineering, ICCE 2000*, *276*, 928–941. https://doi.org/10.1061/40549(276)72

Menter, F. (1993). Zonal Two Equation k-ω Turbulence Models For Aerodynamic Flows. *23rd Fluid Dynamics, Plasmadynamics, and Lasers Conference*. https://doi.org/10.2514/6.1993-2906

Menter, F. R., & Esch, T. (2001). Elements of Industrıal Heat Transfer Predictıons. *16th Brazilian Congress of Mechanical Engineering*, 117-127.

Menter, F. R., Kuntz, M., & Langtry, R. (2003). Ten Years of Industrial Experience with the SST Turbulence Model. *Turbulence, Heat and Mass Transfer 4*.

Mirjalili, B. S., Jain, S. S., & Dodd, M. S. (2017). Interface-capturing methods for two-phase flows : An overview and recent developments. *Center for Turbulence Research: Annual Research Briefs*, *1*, 117–135.

Movahedi, A., Kavianpour, M., & Aminoroayaie Yamini, O. (2017). Experimental and numerical analysis of the scour profile downstream of flip bucket with change in bed material size. *ISH Journal of Hydraulic Engineering*, *25*(2), 188–202. https://doi.org/10.1080/09715010.2017.1398111

Neyshabouri, S. A. A. S., Ferreira Da Silva, A. M., & Barron, R. (2003). Numerical simulation of scour by a free falling jet. *Journal of Hydraulic Research*, *41*(5), 533–539. https://doi.org/10.1080/00221680309499998

Nichols, R. H., & Nelson, C. C. (2004). Wall function boundary conditions including heat transfer and compressibility. *AIAA Journal*, *42*(6), 1107–1114. https://doi.org/10.2514/1.3539

Niemann, S. L., Fredsøe, J., & Jacobsen, N. G. (2011). Sand Dunes in Steady Flow at Low Froude Numbers: Dune Height Evolution and Flow Resistance. *Journal of Hydraulic Engineering*, *137*(1), 5–14. https://doi.org/10.1061/(asce)hy.1943-7900.0000255

Prandtl, L. (1910). Eine Beziehung zwischen Wiirmeaustausch und Stromungswiderstand der Fliissigkeit, *Z. Physik*, 1072-1078.

Qu, S., Liu, S., & Ong, M. C. (2021). An evaluation of different RANS turbulence models for simulating breaking waves past a vertical cylinder. *Ocean Engineering*, *234*, 109195. https://doi.org/10.1016/j.oceaneng.2021.109195

Reichardt, H. (1951). Vollstandige Darstellung der turbulenten Geschwindigkeitsverteilung in glatten Leitungen, *Z. angew. Math. Mech*., 208-219.

Rannie, W. D. (1956) Heat Transfer in Turbulent Shear Flow, *Journal of the Aeronautical Sciences*, 485.

Roache, P. J. (1998). Verification of codes and calculations. *AIAA Journal*, *36*, 696–702. https://doi.org/10.2514/3.13882

Rodi, W. (2017). Turbulence Modeling and Simulation in Hydraulics: A Historical Review. *Journal of Hydraulic Engineering*, *143*(5), 03117001. https://doi.org/10.1061/(asce)hy.1943-7900.0001288

Roenby, J., Bredmose, H., & Jasak, H. (2016). A computational method for sharp interface advection. *Royal Society Open Science*, *3*(11). https://doi.org/10.1098/rsos.160405

Roulund, A., Sumer, B. M., Fredsøe, J., & Michelsen, J. (2005). Numerical and experimental investigation of flow and scour around a circular pile. *Journal of Fluid Mechanics*, *534*, 351–401. https://doi.org/10.1017/S0022112005004507

Saffman, P.G. (1970). Model for Inhomogeneous Turbulent Flow. *Proceedings of the Royal Society*, *317*(1530), 417–433. https://doi.org/10.1098/rspa.1970.0125

Schäffer, H. A., & Klopman, G. (2000). Review of Multidirectional Active Wave Absorption Methods. *Journal of Waterway, Port, Coastal, and Ocean Engineering*, *126*(2), 88–97. https://doi.org/10.1061/(asce)0733-950x(2000)126:2(88)

Schmocker, L., & Hager, W. H. (2010). Overtopping and breaching of dikes – Breach profile and breach flow. *Intl. Conf. River Flow*, *3*, 515–522. https://izw.baw.de/e-medien/river-flow-2010/PDF/A4/A4_01.pdf

Shih, T.-H., Povinelli, L. A., Liu, N.-S., Potapczuk, M. G., & Lumley, J. L. (1999). A Generalized Wall Function. *National Aeronautics and Space Administration*, *July*, 1–20.

Skjelbreia, L., & Hendrickson, J. (1960). Fifth Order Gravity Wave Theory. *Proceedings of Coastal Engineering Conference*, 184–96.

Soulsby, R. (1998). *Dynamics of Marine Sands*. Thomas Telford Publishing.

Spalding, D. B. (1961). A Single Formula for the "Law of the Wall". *Journal of Applied Mechanics*, 455-458.

Steendam, G. J., Van Hoven, A., Van der Meer, J., & Hoffmans, G. (2014). Wave Overtopping Simulator Tests on Transitions and Obstacles At Grass Covered Slopes of Dikes. *Coastal Engineering Proceedings*, *1*(34), 79. https://doi.org/10.9753/icce.v34.structures.79

Stive, M. (1994). Mechanics of coastal sediment transport. *Coastal Engineering*, *24*(1–2), 171–172. https://doi.org/10.1016/0378-3839(94)90032-9

Sumer, B. M., Chua, L. H. C., Cheng, N.-S., & Fredsøe, J. (2003). Influence of Turbulence on Bed Load Sediment Transport. *Journal of Hydraulic Engineering*, *129*(8), 585–596. https://doi.org/10.1061/(asce)0733-9429(2003)129:8(585)

Sumer, B. M., Whitehouse, R. J. S., & Tørum, A. (2001). Scour around coastal structures: A summary of recent research. *Coastal Engineering*, *44*(2), 153–190. https://doi.org/10.1016/S0378-3839(01)00024-2

Sun, R., & Xiao, H. (2016). SediFoam: A general-purpose, open-source CFD-DEM solver for particle-laden flow with emphasis on sediment transport. *Computers and Geosciences*, *89*, 207–219. https://doi.org/10.1016/j.cageo.2016.01.011

Svendsen, I. A. (2006). *Introduction to Nearshore Hydrodynamics*. World Scientific.

Taylor, G. I. (1916). Conditions at the Surface of a Hot Body Exposed to the Wind, *Brit. Aero. Res. Comm*.

Tsujimoto, G., Mineura, R., Yamada, F., Kakinoki, T., & Uno, K. (2014). Scouring Mechanism Behind Seawall from Tsunami Overflow and Optimum Conditions to Reduce Tsunami Energy with an Artificial Trench. *Coastal Engineering Proceedings*, *1*(34), 38. https://doi.org/10.9753/icce.v34.structures.38

van der Meer, J. W., Verhaeghe, H., & Steendam, G. J. (2009). The new wave overtopping database for coastal structures. *Coastal Engineering*, *56*(2), 108–120. https://doi.org/10.1016/j.coastaleng.2008.03.012

van Driest, E. R. (1956). On Turbulent Flow Near a Wall. *Journal of the Aeronautical Sciences*, *23*(11), 1007–1011. https://doi.org/10.2514/8.3713

van Gent, M. R. A. (1995). Wave interaction with permeable coastal structures. *Communications on Hydraulic & Geotechnical Engineering - Delft University of Technology*, *95–5*. https://doi.org/10.1016/0148-9062(96)81968-1

van Gent, M. R., & Pozueta, B. (2005). Rear-Side Staility of Rubble Mound Structures. *Coastal Engineering 2004*. https://doi.org/10.1142/9789812701916_0281

van Gent, M. R. A. (2009). Rear-Side Stability of Rubble Mound Structures with Crest Elements. *Coastal Structures 2007*. https://doi.org/10.1142/9789814282024_0002

Vanneste, D. F. A., Altomare, C., Suzuki, T., Troch, P., & Verwaest, T. (2014). Comparison of Numerical Models for Wave Overtopping and Impact on a Sea Wall. *Coastal Engineering Proceedings*, *1*(34), 5.

https://doi.org/10.9753/icce.v34.structures.5

von Karman, T. (1939). The Analogy Between Fluid Friction and Heat Transfer, *Trans. ASME*, 705-710.

Warmink, J. J., Van Bergeijk, V. M., Chen, W., Van Gent, M. R. A., & Hulscher, S. J. M. H. (2018). Modelling Wave Overtopping for Grass Covers and Transitions in Dike Revetments. *Coastal Engineering Proceedings*, *36*, 53. https://doi.org/10.9753/icce.v36.papers.53

Whitaker, S. (1996). The Forchheimer equation: A theoretical development. *Transport in Porous Media*, *25*(1), 27–61. https://doi.org/10.1007/BF00141261

Whitaker, S. (2010). *The Method of Volume Averaging (Theory and Applications of Transport in Porous Media, 13)*. Springer.

Wilcox, D. C. (2006). *Turbulence Modeling for CFD* (3rd ed.). D C W Industries.

Wilcox, D. C. (1988). Reassessment of the scale-determining equation for advanced turbulence models. *AIAA Journal*, *26*(11), 1299–1310. https://doi.org/10.2514/3.10041

Wilcox, D. C. (2008). Formulation of the k-ω turbulence model revisited. *AIAA Journal*, *46*(11), 2823–2838. https://doi.org/10.2514/1.36541

Yaman, M. (2022). Scour at the Rear Side of Rubble Mound Revetments due to Solitary Wave Overtopping. [Unpublished master's thesis], Middle East Technical University.

Yildirim, E. (2021). Scour at the Rear Side of Rubble Mound Revetments. *Master's Thesis*, Middle East Technical University.